A global 30-m dataset of young forest age for natural and planted forests (1985–2024)

Yan Wang[1], Hengbin Wang[1], Chaoran Liang[1], Xiyi Li[1], Zhe Liu[1,2,3], Xiaodong Zhang[1,2,3], Shaoming Li[1,2,3], Jinming Yang[4], Yuanyuan Zhao[1,2,3]

[1]College of Land Science and Technology, China Agricultural University, Beijing 100083, China; wangyan@cau.edu.cn; hbwang@cau.edu.cn; s20253213945@cau.edu.cn; lixiyi@cau.edu.cn; liuz@cau.edu.cn; zhangxd@cau.edu.cn; lshaoming@sina.com; jinming0221@qau.edu.cn; zhaoyuanyuan@cau.edu.cn.
[2]Key Laboratory of Remote Sensing for Agri-Hazards, Ministry of Agriculture and Rural Affairs, Beijing 100083, China.
[3]Key Laboratory for Agricultural Land Quality, Ministry of Natural Resources of the People's Republic of China, Beijing 100083, China.
[4]Qingdao Agricultural University，No. 700 Changcheng Road, Chengyang, Qingdao, Shandong, China. P.C. 266109

Address correspondence to: Yuanyuan Zhao (zhaoyuanyuan@cau.edu.cn)

Abstract: Natural and planted forests differ substantially in ecological functions and economic values, with forest age serving as a key indicator of their developmental and carbon dynamics. However, existing global forest age datasets remain constrained by coarse spatial resolutions and a lack of explicit distinction between forest origins. In this study, we developed a 30-m global young forest age dataset (1985-2024) by integrating Landsat time series with the Continuous Change Detection and Classification (CCDC) algorithm on Google Earth Engine. To capture the divergent successional trajectories of natural forests (NF) and planted forests (PF), we implemented a dual-threshold segment-fusion logic. Guided by a global forest mask, this framework applies tailored regrowth slope thresholds (>0.03 for NF and >0.04 for fast-growing PF) to fuse successional segments, back-propagating the age estimation to the true biological onset of recovery and minimizing premature spectral resets. We also generated a pixel-level Spatial Uncertainty Index (SUI) based on model residuals. Global validation against extensive reference points confirmed high predictive accuracy (R^2=0.74, RMSE=7.17 years). Globally, pronounced regional contrasts were observed: old-growth NF dominate in Europe (84.38%), South America (82.61%), and North America (80.62%), whereas Australia exhibits a bimodal age distribution driven by both mature and regenerating stands. PF, by contrast, are consistently younger, with the youngest plantations concentrated in Australia (Age 1-5: 65.77%) and the most mature in Europe (Age 36-40: 53.99%). This 30 m global forest age map provides a consistent and high-resolution benchmark for improving forest carbon accounting, plantation yield modeling, and conservation strategy development.

1 Introduction

Forests represent one of the most vital ecosystems on Earth, covering approximately 31% of the global land surface and providing habitats for most terrestrial species (FAO 2024). They play a central role in regulating the global carbon cycle, storing nearly 296 billion tons of carbon and contributing to climate stability, hydrological balance, and biodiversity

conservation (FAO 2024; Murphy et al., 2025; Noss 1999; Thompson et al., 2009). Beyond ecological functions, forests supply wood, fiber, fuel, and food, supporting the livelihoods of billions of people worldwide (Oldekop et al., 2020; Steel et al., 2024). In the context of accelerating climate change and global sustainability challenges, characterizing forest structure and dynamics—particularly forest stand age—has become indispensable for assessing carbon sequestration potential, guiding restoration efforts, and ensuring long-term ecological and social resilience (Erdozain et al., 2024; Leng et al., 2024; Tian et al., 2024; Zhang et al., 2023).

Stand age represents one of the most critical dimensions differentiating NF and PF in terms of growth characteristics and carbon sequestration capacity (Köhl et al., 2017; Liang et al., 2022). PF typically exhibit uniform age structures, with vegetation and soil carbon storage increasing continuously with age. However, their total carbon accumulation is generally lower and highly dependent on management regimes (Cao et al., 2025; Zou et al., 2023). In contrast, NF possess longer growth cycles and complex age distributions; their carbon sequestration rate tends to stabilize after maturity, resulting in higher total carbon stocks and richer ecosystem functions (He et al., 2022; Liang et al., 2022; Liao et al., 2023; Shi et al., 2022). These divergent age-carbon relationships introduce significant uncertainties in carbon sink estimation when using models such as the Integrated Terrestrial Ecosystem C-budget (InTEC) model (Chen et al., 2000). Accurate information on both forest type and age is therefore essential for improving carbon accounting precision and guiding evidence-based forest management (Cheng et al., 2024b; Mo et al., 2024). To fully assess the contribution of both forest types to climate mitigation and biodiversity conservation, mapping their age distributions at the global scale is of paramount importance (Aszalós et al., 2022).

The evolution of forest age estimation has transitioned through multiple remote sensing paradigms. Early statistical models and image classification approaches frequently struggled to capture complex nonlinear relationships or faced spectral saturation in heterogeneous landscapes (Reyes-Palomeque et al., 2021). Remote sensing inversion methods, including K-Nearest Neighbor and Random Forest regression, were introduced to better capture these nonlinearities; however, they remain vulnerable to overfitting when applied across diverse and complex ecosystems (Tang et al., 2020). To circumvent these issues, multi-sensor fusion—utilizing synthetic aperture radar's (SAR's) canopy penetration and LiDAR's vertical structural profiling—has provided high-precision regional benchmarks (Champion et al., 2013; Racine et al., 2014; Trisasongko et al., 2020). Nevertheless, the prohibitive costs and sparse temporal coverage of LiDAR, coupled with terrain-induced noise in SAR, have restricted their application for continuous global monitoring. Consequently, with the opening of the Landsat archive, time-series algorithms like LandTrendr and the Continuous Change Detection and Classification (CCDC) have become the preferred frameworks. By analyzing pixel-level spectral trajectories, these approaches can track both abrupt disturbances and gradual recovery, offering a physically-based estimation of forest establishment (Du et al., 2022; Li et al., 2024; Xiao et al., 2023).

Despite these methodological advancements, a gap exists between global monitoring needs and currently available products. Foundational datasets like the Global Forest Age Dataset (GFAD) rely on national inventories and biomass-age relationships but lack the spatial resolution (0.5°) to capture the fragmented forest patches characteristic and mosaic landscapes prevalent in the satellite era (Poulter et al., 2018). Subsequent efforts have pushed the resolution boundaries, notably the 1-km global

dataset developed by Besnard et al. (2021) and its 100-m successor, the Global Age Mapping Integration (GAMI) (Besnard et al., 2024). However, while GAMI represents a major leap in spatial detail, these products often depend on static snapshots or biomass-inversion rather than explicit, multi-decadal change detection. More recently, Du et al. (2022) created a 30 m-resolution global dataset of planting years of plantation (PYP) based on Landsat time-series analysis, offering higher spatial detail but focusing solely on PF. At national scales, 30-m mapping has achieved success in regions like Canada (Maltman et al., 2023), Europe (Vilén et al., 2012), and China (Zhang et al., 2017), yet these efforts are often hindered by disparate inventory standards that prevent global harmonization. Crucially, as summarized in Table 1, existing different resolution products—including the global PYP dataset which focuses exclusively on plantations—rarely distinguish between NF and PF, leaving a critical blind spot in our understanding of natural forest dynamics.

Table 1. Comparison of major global and regional forest age products

Dataset / Study	Spatial resolution	Extent	Distinguish NF and PF	Data source	Methods
GFAD (Poulter et al., 2018; Poulter et al., 2019)	0.5 °	Global	No	MODIS Collection 5.1 land cover dataset, national inventories, and biomass data	Statistical mapping of age-class fractions
GAMI(Besnard et al., 2024)	100 m	Global	No	Disturbance data, climate data, field surveys	Random forest
Planting years of plantation (Du et al., 2022)	30 m	Global	Only PF	Landsat imagery, SDPT	LandTrendr
Vilén et al., (2012)	0.25 °	Europe	No	Country-level historical age-class data,	Backcasting model
Zhang et al., (2017)	1km	China	No	Forest height data, forest type data, climate data, field survey	Growth model
Shang et al., (2023)	30 m	China	No	Landsat imagery, forest height, elevation, field surveys	Continuous change detection, machine learning
Cheng et al., (2024a)	30 m	China	No	Landsat imagery, canopy height, climate data, soil data, elevation, and field surveys	LandTrendr, Machine Learning

Xiao et al., (2023)	30m	China	No	Landsat imagery, land cover masks	CCDC
Maltman et al., (2023)	30 m	Canada	No	Landsat imagery, MODIS GPP data, field surveys, fire data	Multi-epoch (Change detection + Allometry)
Pan et al., (2011)	1 km	North America	No	SPOT imagery, landcover classification, disturbance records, field surveys	Disturbance detection
Li et al., (2024)	30m	Loess Plateau (China)	Only PF	Landsat imagery	LandTrendr

While these diverse approaches offer complementary advantages—ranging from the local-scale precision of inversion models to the temporal continuity of time-series algorithms—significant barriers to global, high-resolution forest age mapping remain. First, the majority of extant large-scale datasets lack the spatial resolution necessary to capture fine-scale age heterogeneity in fragmented landscapes (Smolina et al., 2023). Second, the failure to differentiate between NF and PF in most products undermines the reliability of carbon sequestration estimates, given their contrasting age-carbon trajectories (Su et al., 2023; Yu et al., 2024). Third, the geographic or functional confinement of existing 30-m products to specific regions or single forest types limits their applicability for global-scale carbon accounting (Besnard et al., 2021; Huang et al., 2023; Lu et al., 2025; Maza et al., 2021). Consequently, a comprehensive global forest age dataset that integrates high spatial resolution, explicit forest type differentiation, and consistent worldwide coverage remains absent.

To address these gaps, this study develops a globally consistent, 30-m resolution forest age dataset that explicitly distinguishes between NF and PF. Leveraging the Google Earth Engine (GEE) platform, we implemented the CCDC algorithm on Landsat 4-8 archives (1985-2024) to track pixel-level forest dynamics. A key methodological advancement of our approach is the integration of a prior-informed semantic merging logic. By incorporating forest-type-specific growth constraints derived from the Global Natural and Planted Forests (GNPF) dataset, we consolidated biologically continuous segments that are frequently misidentified by standard CCDC fitting as discrete disturbance events. This refinement ensures that the estimated age accurately reflects the true duration of stand development rather than spectral artifacts of canopy closure.

2 Datasets and methods

The workflow of this study includes four main stages (Fig. 1). First, a multi-decadal Landsat NBR time series (1985-2024) was constructed and harmonized using the GEE platform. Second, the CCDC algorithm was employed to perform synergistic temporal segmentation, decomposing the spectral trajectories into discrete, homogeneous segments, while the GNPF dataset was integrated to provide thematic baselines. Third, a category-specific segment-fusion logic was implemented to reconcile

spectral stabilization lags and back-propagate the establishment year based on the distinct regrowth characteristics of each forest type, complemented by a pixel-wise Root Mean Square Error (RMSE) analysis to quantify model uncertainty. Finally, the estimated young forest age—specifically defined as the time elapsed since the most recent detectable stand-replacing disturbance—was rigorously validated using a multi-source evidence synthesis framework.

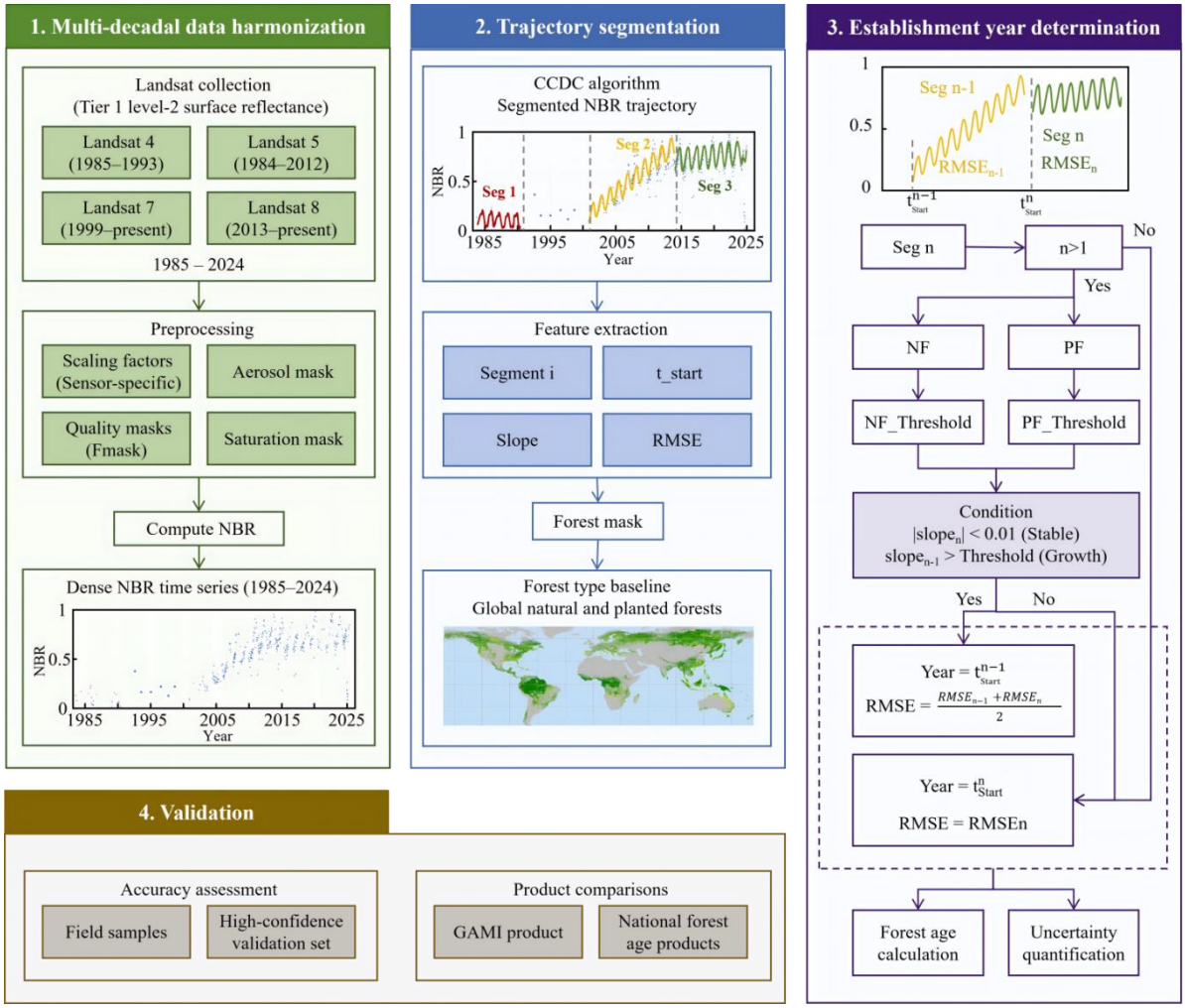

Figure 1: Workflow of estimating forest age for global natural and planted forests.

2.1 Global natural and planted forests dataset

The GNPF dataset provides the global distribution of natural and planted forests at 30 m spatial resolution for 2021 (Xiao et al., 2024). Derived from Landsat time-series imagery (1985-2021), the dataset distinguishes forest types based on differences in disturbance frequency, achieving an overall accuracy (OA) of 85%. The proportions of forest types are consistent with the FAO's Global Forest Resources Assessment 2020, ensuring high thematic reliability. The GNPF dataset was used to generate

a forest type mask that separates natural and planted forest pixels. This mask served as a spatial reference for forest age estimation, enabling independent analysis of temporal dynamics for each forest type.

2.2 Time series construction and data harmonization

A multi-decadal Landsat time series (1985-2024) was constructed by leveraging the extensive data catalog of the GEE platform. We ingested all available Tier 1 Level-2 surface reflectance products from Landsat 4, 5, 7, and 8 (TM, ETM+, and OLI sensors). These products were preprocessed using the LEDAPS and LaSRC algorithms for radiometric calibration and atmospheric correction (Ju et al., 2012; Vermote et al., 2018). To ensure a high-quality temporal stack, we implemented rigorous quality masking—including QA_PIXEL for cloud and shadow removal, alongside aerosol and saturation filters. Furthermore, to maintain radiometric consistency across generations of sensors, Landsat 8 reflectance values were normalized to match the ETM+ sensor using established scaling factors.

Vegetation indices are sensitive indicators of canopy condition and ecosystem successional dynamics. In this study, the Normalized Burn Ratio (NBR) was selected as the core spectral indicator due to its high responsiveness to both abrupt canopy loss and gradual post-disturbance recovery (Bright et al., 2019; Escuin et al., 2008; Ryu et al., 2018). NBR, calculated from the Near-Infrared (NIR) and Shortwave Infrared (SWIR2) bands, effectively captures structural and moisture changes in vegetation, making it particularly suitable for detecting forest loss and regrowth following disturbances such as fire or logging. The NBR is calculated as follows:

$$\mathrm{NBR}=\frac{\mathrm{NIR\text{-}SWIR2}}{\mathrm{NIR+SWIR2}}, \tag{1}$$

2.3 Trajectory segmentation and parameter extraction

The CCDC algorithm was executed to decompose the 40-year NBR time series into discrete, chronologically homogeneous segments. This algorithm fits a robust harmonic regression model—incorporating long-term trend and intra-annual seasonal components—via ordinary least squares (OLS) to capture steady-state land surface behavior. Land surface modifications or abrupt disturbances are flagged when a sequence of consecutive observations deviates substantially from the predicted model boundaries beyond a specified statistical threshold (chiSquareProbability < 0.99, Table 2). The mathematical formulation of the CCDC fitting model is expressed as follows:

$$\hat{\rho}(i,x)=a_{0,i}+a_{1,i}\cos\frac{2\pi x}{T}+b_{1,i}\sin\frac{2\pi x}{T}+a_{2,i}\cos\frac{2\pi x}{NT}+b_{2,i}\sin\frac{2\pi x}{NT} \tag{2}$$

Where $\hat{\rho}(i,x)$ represents the predicted value of the i-th band of fitted Julian date x; i represents the i-th spectral band; T represents the number of days in each year; $a_{0,i}$ represents the total value of the i-th band reflectance; $a_{1,i}$ and $b_{1,i}$ represent the coefficient of the intra-annual variation term of the reflectance of the i-th band; $a_{2,i}$ and $b_{2,i}$ represent coefficients for inter-annual change for the i-th band; N represents number of years.

For each successfully initialized model segment, critical temporal attributes were extracted: the model initialization time (t_{Start}), segment end time, the slope (denoting the spectral recovery or degradation rate), and the RMSE. Crucially, t_{Start} signifies the exact temporal anchor where a new harmonic model stabilizes post-disturbance. For pixels exhibiting zero structural breakpoints across the entire 1985-2024 archive, the entire timeline was cataloged as a single stable segment, establishing the baseline for old-growth forest delineation (≥ 40 years). The principal execution parameters for CCDC are detailed in Table 2.

Table 2. Parameter settings for CCDC in this study.

Input	Parameters
breakpointBands	'GREEN', 'RED', 'NIR', 'SWIR1', 'SWIR2','NBR'
tmaskBands	'GREEN', 'SWIR2'
minObservations	6
chiSquareProbability	0.99
minNumOfYearsScaler	1.33
dateFormat	1
lambda	0.002
maxIterations	10000

2.4 Young forest age estimation

2.4.1 Category-specific adaptive segment-fusion logic

Recognizing that these forest types exhibit divergent successional trajectories—where plantations typically undergo accelerated canopy closure compared to the more stochastic recovery of natural stands—we implemented a dual-threshold segment-fusion logic. This approach utilizes the GNPF mask as a spatial constraint during the algorithmic execution phase, thereby ensuring that the biological characteristics of each forest type directly govern the age estimation process. The fusion logic was specifically designed to reconcile the systematic lag between the initial disturbance and the stabilization of the subsequent spectral model, as illustrated in Stage 3 of the framework (Fig. 1). To avoid arbitrary parameterization, the baseline fusion thresholds for each forest category were directly informed by the underlying statistical distributions of our historical reference data. For NF, the framework identifies the transition from a rapid successional phase to a steady state; if a terminal stable segment ($|slope| < 0.01$) is preceded by a regrowth segment with a slope exceeding 0.03, the segments are fused to back-propagate the establishment year to the true onset of recovery. Conversely, for PF, a more stringent regrowth threshold ($slope > 0.04$) is enforced to account for the aggressive spectral shifts characteristic of fast-growing plantation species. By tailoring these thresholds to the specific recovery rates of NF and PF, the model effectively minimizes the underestimation of young forest age caused by premature spectral resets.

2.4.2 Age qualification and reliability mapping

The final young forest age was calculated by subtracting the validated establishment year of the terminal sequence from the reference year (2024). For pixels where the spectral trajectory remained stable throughout the entire 1985-2024 observation window, indicating no stand-replacing disturbances within the Landsat record, they were assigned to an age class of ≥ 40 years. To provide a spatially explicit assessment of the product's reliability, we generated a pixel-wise uncertainty map based on the RMSE. This metric is dynamically coupled with our segment-fusion logic: for pixels where no fusion occurred, the RMSE of the terminal stable segment was utilized; for pixels where rapid-growth and steady-state segments were fused, the uncertainty was calculated as the weighted average RMSE across both segments. By linking uncertainty directly to the trajectory fitting quality, we allow users to identify regions where complex sub-pixel dynamics or residual atmospheric noise may impact the precision of the age estimates.

2.4.3 Adaptive grid partitioning across global continents

To ensure computational efficiency and facilitate large-scale processing, an adaptive grid partitioning scheme was developed based on the Large Scale International Boundary (LSIB) dataset from the U.S. Department of State's Office of the Geographer and Global Positioning Systems (2017). The dataset, which integrates and simplifies global administrative boundaries while maintaining essential regional distinctions, provides sufficient spatial precision for continental-scale analysis. Using the "Continental Region" layer of the LSIB, the global landmass was divided into spatial units for independent CCDC processing. As the GNPF dataset did not predict any forest cover in the South Atlantic, Antarctica, and Greenland (within the North American region), these areas were excluded from subsequent analyses. This exclusion reduced computational redundancy and prevented interference from invalid grids, thereby enhancing global processing efficiency.

2.5 Validation samples generation

To rigorously evaluate the accuracy of forest age estimates, we established a validation framework integrating high-resolution imagery with dense spectral time-series trajectories (Fig. 2). The global land surface was first partitioned into 57,559 independent $0.5° \times 0.5°$ grid cells to ensure spatial representativeness. Within each grid, a stratified random sampling strategy was applied to select five samples for both natural and planted forests, achieving global spatial uniformity and avoiding clustering.

The reference forest age for each sample was determined through a multi-evidence manual interpretation protocol. We integrated Google Earth historical high-resolution imagery, annual Landsat-derived spectral trajectories (NBR and NDVI), and the Global Forest Change (GFC) dataset to cross-verify the timing of disturbance and regeneration events. In this framework, the GFC loss year provided an initial objective benchmark for disturbance timing. This was then cross-referenced with Landsat spectral breakpoints to pinpoint the onset of the current growth cycle, while Google Earth imagery provided supplementary spatial verification of canopy establishment. To address the limitations of inconsistent image quality and

temporal gaps in Google Earth (particularly for the 1985-2000 period), an establishment year was confirmed only when the evidence from spectral trajectories, GFC records, and available spatial imagery reached a consensus. For ambiguous cases—such as pixels with persistent cloud cover, blurry historical snapshots, or unclear natural regeneration signals—the samples were excluded to maintain a high-confidence validation set. Ultimately, we obtained 8085 forest age samples, including 4021 NF samples and 4064 PF samples.

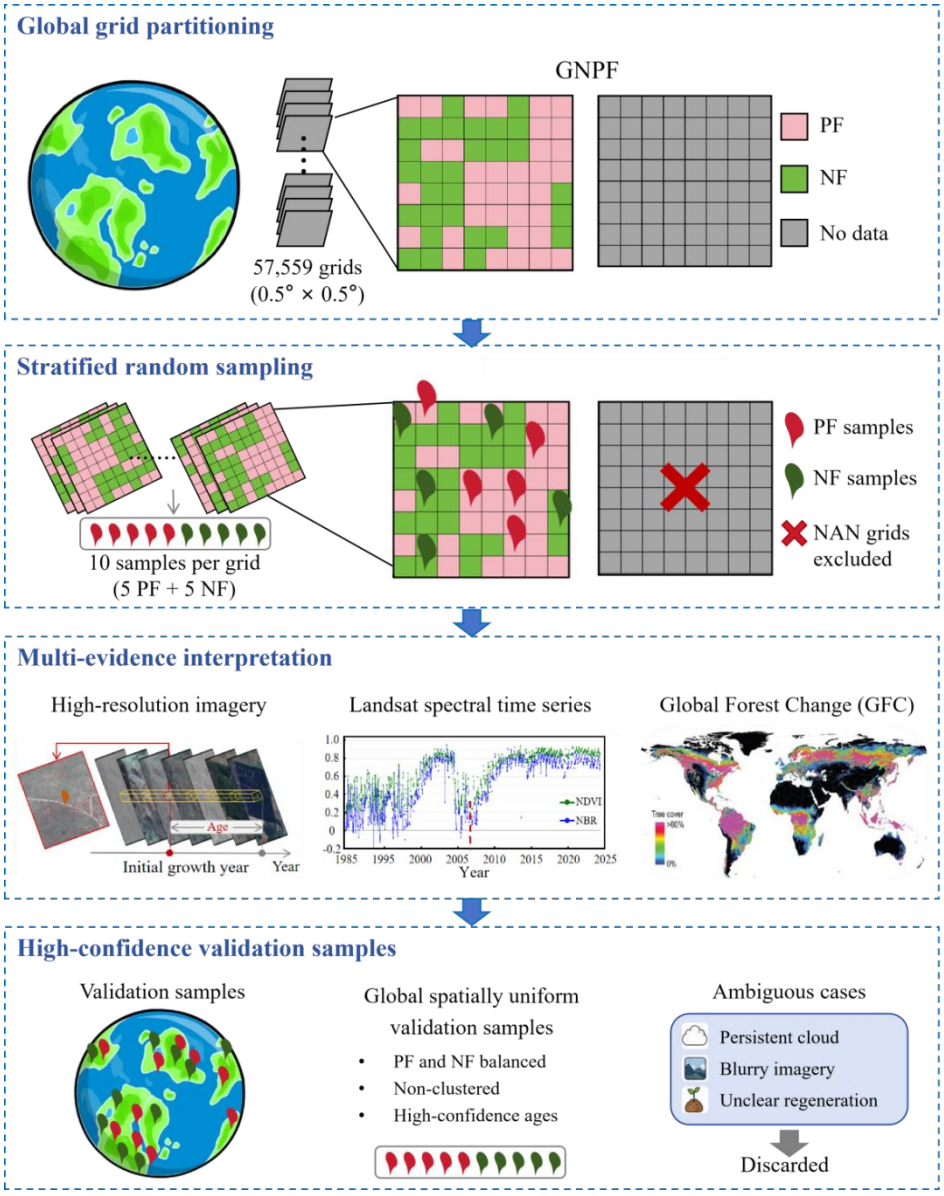

Figure 2: Workflow for generating validation samples using global grid-based stratified sampling.

3 Results

3.1 Forest age accuracy

3.1.1 Model performance and predictive accuracy

To rigorously assess the accuracy of our global forest age product, we conducted a comprehensive validation using a total of 8,365 samples (Fig. 3a). This validation database comprises 8,085 high-confidence interpreted samples generated through our multi-evidence protocol (as described in Section 2.5) and 280 independent field survey samples, which serve as an independent ground-truth source to supplement the interpretation-based validation.

On a global scale, the model exhibited high consistency with these multi-source validation data, achieving a coefficient of determination (R^2) of 0.74 and an RMSE of 7.17 years (Fig. 3c). The density scatter plot illustrates that most predicted values are tightly clustered along the 1:1 line, indicating that the CCDC-based framework can accurately capture forest age across various successional stages. While the variance slightly increases for older forest stands—likely due to the inherent limitation of spectral saturation—the overall accuracy remains high, demonstrating the model's reliability for global-scale applications.

The validation accuracy was further analyzed across different forest origins and climatic zones (Fig. 3d). When evaluated by forest origin, the model demonstrated substantially stronger explanatory power for PF (R^2 = 0.78, RMSE = 7.00 years) than for NF (R^2 = 0.64, RMSE = 7.34 years). This difference reflects the relatively simpler stand structures and more distinct disturbance-recovery signals in plantations. Furthermore, climatic zone statistics revealed distinct spatial variations in model performance. The model achieved highly stable segment-fitting results in temperate and boreal regions, where seasonal phenological cycles and discrete disturbance events (e.g., clear-cutting, wildfires) are clearly defined in the Landsat time series. In contrast, time-series regressions in tropical regions were inherently subject to greater fitting volatility, which can be attributed to persistent cloud cover and rapid vegetation regrowth that partially mask long-term spectral trajectories. Overall, the consistent performance across diverse sample types and geographical regions underscores the effectiveness of our approach in quantifying global forest age dynamics.

Despite the robust overall performance, a noticeable saturation effect and increased dispersion were observed in stands exceeding 25 years (Fig. 3c). In this high-age interval, the model exhibited a systematic underestimation tendency, with predicted values frequently falling below the 1:1 line. This deviation highlights an inherent sensitivity threshold in the current estimation framework for mature forest structures.

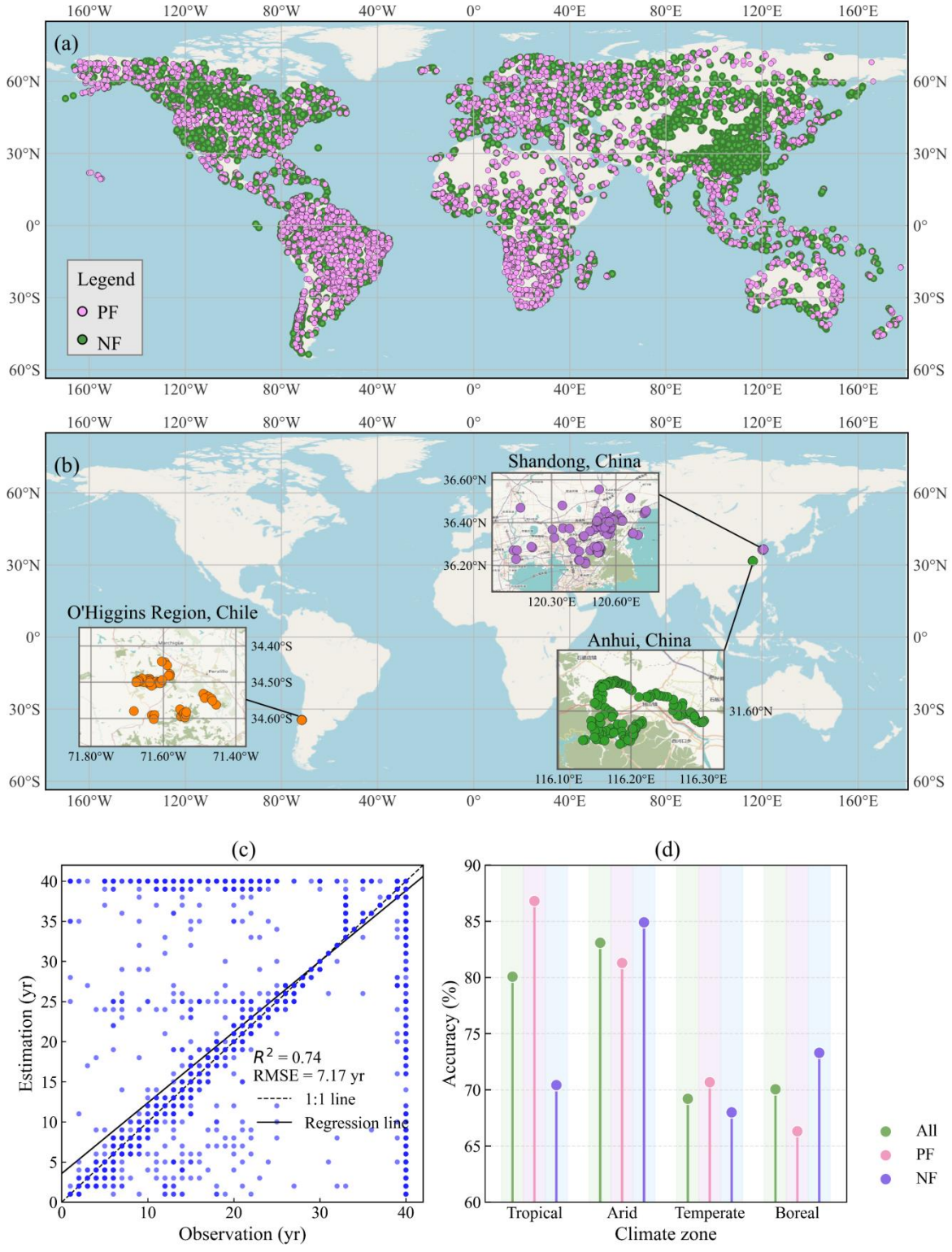
(a)
Legend
PF
NF
(b)
Shandong, China
O'Higgins Region, Chile
Anhui, China
(c)
Estimation (yr)
Observation (yr)
R^2 = 0.74
RMSE = 7.17 yr
1:1 line
Regression line
(d)
Accuracy (%)
Tropical
Arid
Temperate
Boreal
Climate zone
All
PF
NF

Figure 3: Validation sample distribution and accuracy verification of forest age prediction model. (a) The global distribution of all validation samples. (b) The global distribution of field samples. (c) Scatter plot and fitting relationship between observed and predicted forest ages. (d) Accuracy comparison across climate zones and sample types. NF represents natural forest, PF represents planted forest, and All represents the combination of the two types of forests.

To assess the reliability of the forest age estimates, we compared our product—the Global 30m Forest Age Map (Natural vs. Planted) (GFAM-N/P)—with a 30 m-resolution forest age product (FAP) developed by Xiao et al. for China (2023). The reference dataset identifies forest establishment years from 1990 to 2020, whereas our study extends the temporal coverage to 1985-2024. Despite this difference, both datasets exhibited strong agreement in forest age estimation within the overlapping period.

To ensure fair comparison, we performed stratified random sampling within the overlapping forested area based on China's climatic regionalization (Fig. 4a). Specifically, 100 samples were selected from each of the tropical monsoon, temperate continental, and alpine plateau climatic zones, and 200 samples from each of the subtropical monsoon and temperate monsoon zones, resulting in 700 uniformly distributed samples across the country (Fig. 4b). Differences in forest age between the two datasets were analyzed using both a difference histogram and Bland-Altman consistency analysis (Bunce 2009). The results showed that the age differences were narrowly distributed and symmetrically centered around 0 (Fig. 4c). The kernel density estimation (KDE) curve displayed a sharp and narrow peak (Terrell et al., 1992), indicating that most samples had minimal deviations in forest age. In the Bland-Altman plot, the mean bias (red dashed line) was close to 0, and 95% of the samples fell within the consistency limits, with only a few isolated outliers (Fig. 4d). These findings demonstrate a high level of consistency between the two products, suggesting that despite differences in temporal span, both share similar methodological logic in forest age extraction and produce comparable results during the overlapping period.

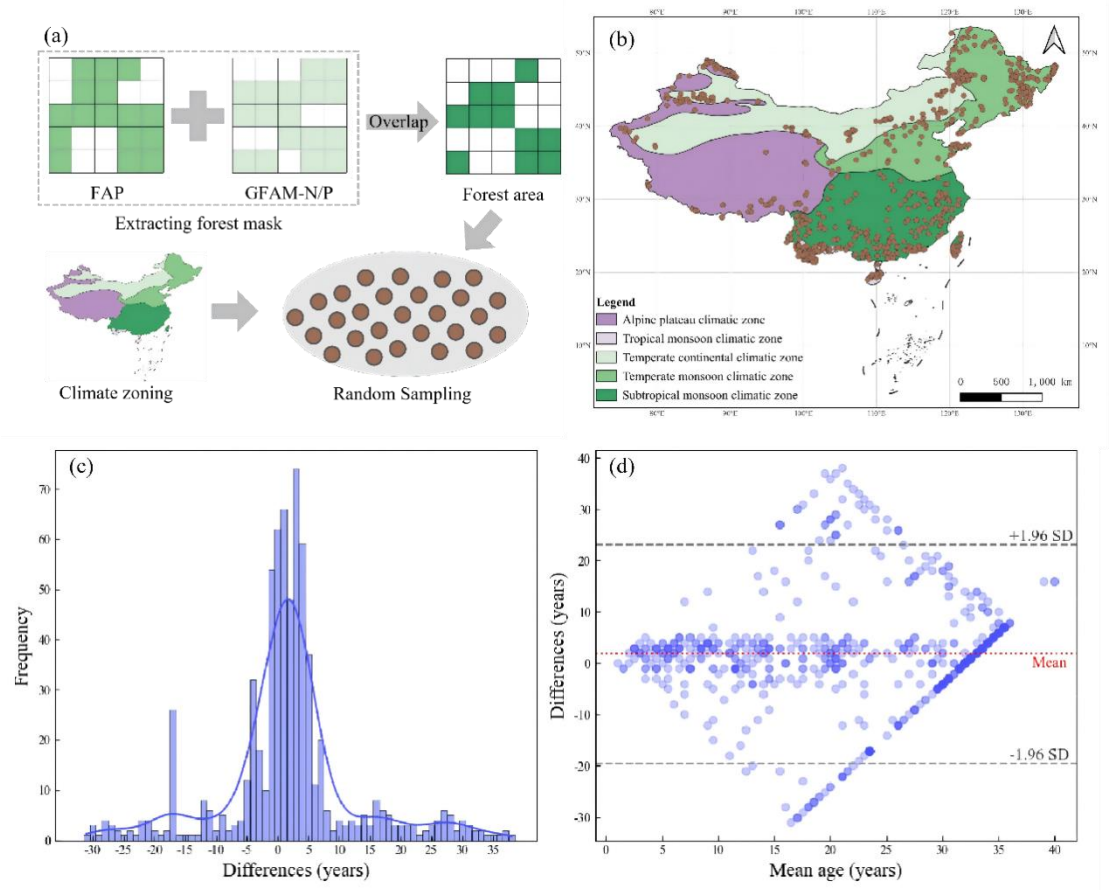

Figure 4: Sample generation, distribution and accuracy assessment. (a) Sample generation. (b) Spatial distribution of samples across climatic zones in China. (c) Distribution of forest age differences between the GFAM-N/P and the FAP (difference = GFAM-N/P − FAP). (d) Bland-Altman plot showing the agreement between the two datasets; the central red line represents the mean difference (bias), and the gray dashed lines indicate the ±1.96 × standard deviation range (95% limits of agreement).

3.1.2 Comparison with existing products

We conducted a visual comparison between the GFAM-N/P and the GAMI dataset developed by Besnard et al., (2024) , which has a spatial resolution of 100 m. Three representative comparison sites are presented to highlight differences in spatial detail and data quality (Fig. 5). At Site 1, the GFAM-N/P resolved highly continuous, fine-scale age gradients across the landscape. In contrast, the coarser 100 m resolution of GAMI limited its ability to capture small and fragmented forest patches, leading to partial or missing age information. At Site 2, where forests dominated the landscape, GAMI failed to delineate forest age across extensive regions. This omission can be attributed not only to its lower spatial resolution but also to its data fusion approach, which likely removed pixels with low inter-source consistency, thereby reducing fine-scale structural details. At Site 3, GAMI depicted only fragmentary forest age patterns, again reflecting limitations associated with its empirical modeling framework. Because the GAMI dataset estimates forest age from the empirical relationship between biomass and stand age,

its accuracy is inherently constrained by input data quality and model assumptions. In contrast, the GFAM-N/P captures spatiotemporal variations in both planted and natural forests at a finer spatial resolution, providing enhanced insights into forest growth dynamics and carbon sequestration potential. This improvement underscores the value of our dataset for precision forest management and carbon cycle monitoring at regional and global scales.

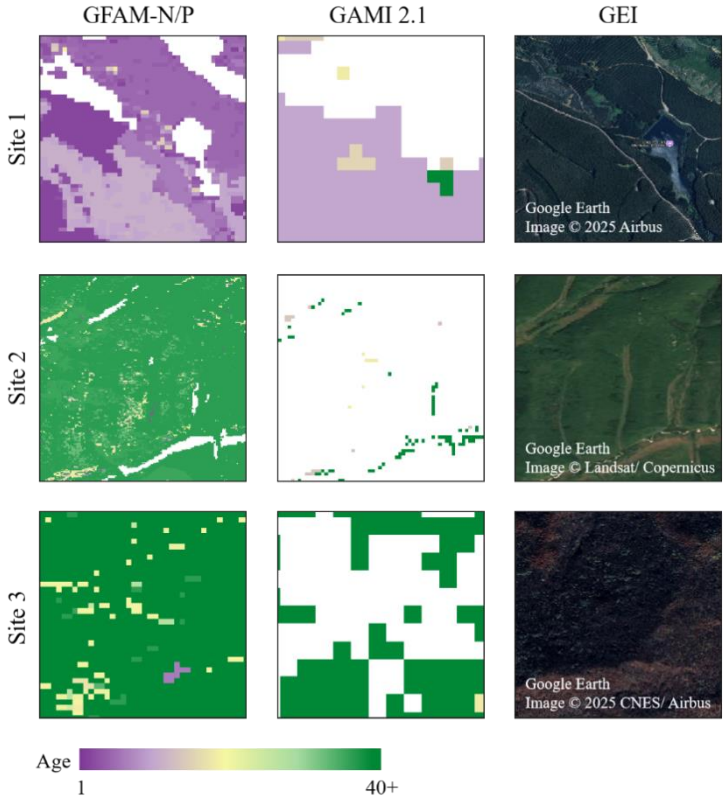

Figure 5: Comparison between the GFAM-N/P and the 100 m-resolution GAMI 2.1 product across three representative sites. White pixels in the forest age maps represent non-forest areas. High-resolution satellite images are from Google Earth (Site 1: Image © 2026 Airbus; Site 2: Image © 2026 Landsat/Copernicus; Site 3: Image © 2026 CNES/Airbus).

To further evaluate the reliability and spatial consistency of our dataset, we conducted an independent cross-validation by comparing our results with the existing GAMI. We employed a spatially stratified random sampling approach to select 50,000 points globally, weighted by the pixel area of the source tiles. To mitigate potential geolocation mismatches and spatial noise between different datasets, a 3×3 median window filter was applied to extract the age value from our product at each sampling location, which was then paired with the single-pixel value from the GAMI product. After rigorously filtering out invalid values, such as NoData and negative pixels in either product, a total of 30,215 valid comparative sample pairs were retained. The continuous forest age values were subsequently categorized into five discrete age intervals (1-10, 10-20, 20-30, 30-39, and ≥ 40 years) to construct a confusion matrix for quantitative assessment.

The cross-comparison reveals a strong overall agreement between our generated product and the GAMI dataset. The OA reached 76.12%, with a Kappa coefficient of 0.67, indicating agreement beyond random chance. Additionally, the weighted F1-score across all classes reached 0.75. These metrics demonstrate a high degree of spatial consistency between the two independent products at the global scale. Detailed class-level performance demonstrates that the highest consistency generally occurs in older forest stands. Specifically, the ≥ 40 years age class exhibited an outstanding user's accuracy (UA) of 93.48%, indicating high reliability when our product identifies mature forests. Concurrently, the 30-39 years class achieved the highest producer's accuracy (PA) of 97.30%, coupled with a robust F1-score of 0.83.

As illustrated in the confusion matrix (Table 3), the majority of discrepancies occurred between adjacent age classes, which is a common and expected phenomenon when binning continuous biophysical variables into discrete intervals. For instance, a notable portion of samples categorized as ≥ 40 years in GAMI were classified into the 30-39 years group in our product. These specific uncertainties may stem from inherent differences in input data sources, spatial resolutions, and the distinct algorithmic definitions of rapid growth stages in young forests utilized by the two datasets. Nevertheless, the confined nature of these discrepancies does not undermine the strong overall accuracy, thereby confirming the global viability and competitive performance of our forest age dataset.

Table 3. Confusion matrix and accuracy assessment between our product and the GAMI product. (Rows represent the reference GAMI data, and columns represent our predicted product. Age class units are in years.)

Age class (years)	1-10	10-20	20-30	30-39	≥40	PA (%)
1-10	1,552	233	232	422	71	61.83
10-20	336	1,065	256	726	113	42.67
20-30	274	165	3,474	738	173	72.01
30-39	69	33	104	10,545	87	97.3
≥40	302	151	718	2,013	6,363	66.65
UA (%)	61.27	64.66	72.62	73.01	93.48	

To thoroughly investigate the geographic variations and explain potential discrepancies between GFAM-N/P and the GAMI dataset, we further cross-evaluated the compliance across four major Köppen climate zones: Tropical, Arid, Temperate, and Boreal (Table 4). The stratified assessment reveals pronounced spatial heterogeneity in product consistency, with OA ranging from 70.09% to 81.35%. The highest spatial consistency was observed in the Arid climate zone (OA = 81.35%, Kappa = 0.73) and the Boreal climate zone (OA = 79.87%, Kappa = 0.70). In the Boreal climate zone, the multi-temporal CCDC algorithm successfully captured historical stand-replacing disturbances (e.g., wildfires and logging) with clear spectral trajectories, which highly aligned with GAMI's biomass-driven estimates in low-productivity environments. For both Arid and Boreal climate zones, the mature forest class (≥ 40 years) demonstrated exceptional reliability, with UA exceeding 87.09% and 95.07% respectively, confirming strong global confidence in delineating undisturbed, older forest stands.

Table 4. Summary of quantitative consistency metrics across different climate zones.

Climate zone	Sample Size	OA	Kappa coefficient	Weighted F1-score
Global all	30,215	76.12%	0.67	0.75
Tropical	7,660	70.09%	0.58	0.70
Arid	4,982	81.35%	0.73	0.80
Temperate	8,369	74.39%	0.64	0.73
Boreal	9,204	79.87%	0.70	0.80

3.1.3 Spatial uncertainty and pixel-level confidence assessment

To fulfill the need for a spatially explicit and quantitative assessment of forest age estimation uncertainty, a pixel-level Spatial Uncertainty Index (SUI) was derived by linearly scaling the RMSE obtained from the time-series CCDC model inversion. The global spatial distribution of this continuous uncertainty layer is illustrated in Fig. 6, where higher SUI values directly correspond to greater spectral fitting residuals and lower mapping confidence. The geographic patterns exhibit pronounced spatial heterogeneity across the globe. Specifically, high-confidence regions characterized by low SUI values (SUI < 5, represented by deep purple and blue pixels) are predominantly clustered in intensively managed forest sectors and plantation zones, such as southeastern China, the southwestern United States, and parts of subtropical southern Africa. In contrast, moderate-to-high uncertainty (SUI ranging from 8 to 13, represented by cyan and green pixels) is clearly visible across the tropical rainforest domains of the Amazon Basin and Central Africa. Notably, several pixel-level hot spots with exceptionally high SUI values (SUI > 12, appearing as yellow pixels) are also scattered within these tropical domains, which are likely driven by persistent cloud contamination and complex multi-layered canopy structures that inevitably elevate model fitting residuals. The maximum mapping uncertainty with the highest SUI values (SUI > 12, represented by yellow pixels) is heavily concentrated along a distinct latitudinal gradient in the temperate and boreal forest sectors across northern North America and northern Eurasia, where shortened growing seasons and snow cover dynamics introduce substantial environmental noise into time-series inversions.

Furthermore, the pixel-level uncertainty layer was rigorously cross-examined against extensive independent ground networks. Quantitatively, validation outcomes across distinct climatic zones confirmed that the estimated forest age exhibits a highly localized and tightly bounded error structure. The Mean Absolute Error (MAE) spanned from a minimum of 1.15 years in tropical domains to 3.84 years in boreal regions, demonstrating strong spatial alignment with the geographic patterns of the SUI, where the Boreal climate zone is inherently characterized by accentuated fitting noise. Crucially, within the designated high-confidence windows (SUI < 5), the actual mapping error remained exceptionally well-constrained, yielding a stable baseline MAE of 2.32 years.

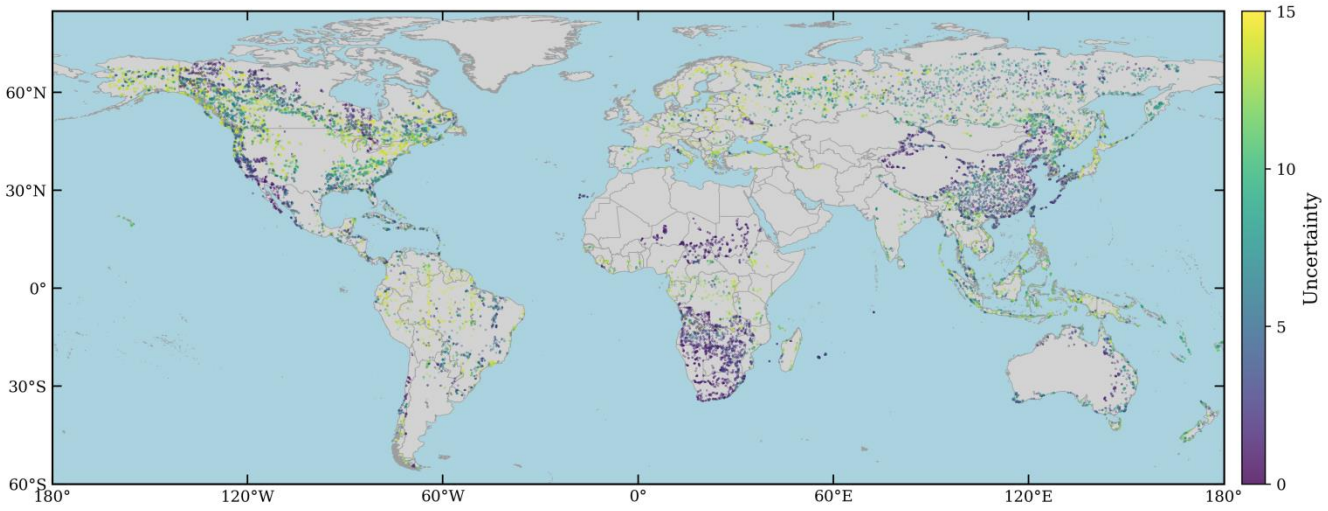

Figure 6: Global spatial distribution of the model-derived SUI for forest age estimation.

3.1.4 Independent validation against forest inventory

To evaluate the localized vertical performance and empirical saturation behavior of our global forest age product, an independent validation framework was constructed using the United States Forest Inventory and Analysis (FIA) database (USDA Forest Service 2024). Nationally distributed plot-level descriptors and stand condition dynamics were cross-linked and integrated across all available states by matching unique plot identifiers. To ensure rigorous data quality, the empirical forest inventory plots were filtered based on three strict criteria: (1) an exact measurement year of 2024, (2) a pure forest condition status, and (3) valid continuous stand age records. From the resulting high-quality georeferenced inventory database, a spatially representative subset of 8,000 plots was randomly subsampled to perform the systematic validation against the model-predicted ages across seven distinct observed age cohorts (Fig. 7).

The box-and-whisker plot demonstrates high linear fidelity within the young and intermediate successional cohorts (Age 1-30). Specifically, the mean predicted age (red line) scales step wisely with the empirical field measurements, exhibiting tightly bounded interquartile ranges in the earliest successional stage (Age 1-10). However, as the observed field stand age surpasses the theoretical observation depth of the multi-decadal Landsat archives ($\geq$ 40 years), a distinct predictive plateau emerges. Within the mature, old-growth, and over-mature classes (Age 40-60, Age 60-100, and Age > 100), the distributions of predicted ages heavily compress and converge immediately below the 40-year maximum threshold (blue dashed line). This asymmetric distribution quantifies the upper boundary conditions of the CCDC-based inversion framework, validating its high-resolution precision for young cohorts while mapping the inevitable saturation baseline in long-term undisturbed forest matrices.

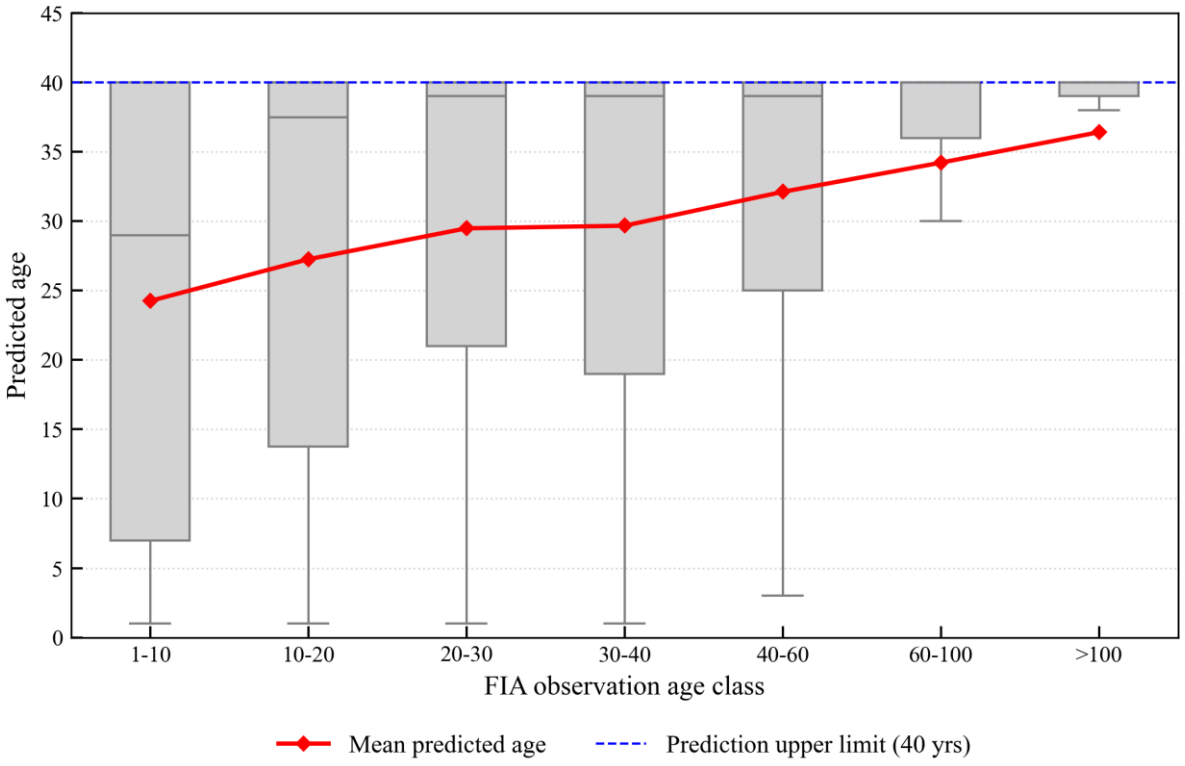

Figure 7: Systematic validation of predicted forest age against independent US FIA plot data across distinct age classes.

3.2 Sensitivity of CCDC configurations to spectral inputs and algorithmic parameters

To evaluate the robustness and global applicability of our CCDC configuration, we conducted systematic sensitivity tests across the four representative Köppen climate zones.

First, we assessed the sensitivity of the minObservations parameter (Fig. 8a). The results indicate that estimation accuracy initially increases with higher observation counts, particularly in the Tropical climate zone where OA improved significantly from 61.61% to 71.27% as the threshold rose from 5 to 8. This confirms that a larger observation window is critical for mitigating persistent cloud interference in humid regions. Ultimately, a uniform value of 6 was selected as a global compromise to balance noise suppression with the capability to detect rapid disturbance events.

Second, the sensitivity to the chiSquareProbability threshold was evaluated (Fig. 8b). Estimation accuracy remains highly sensitive to this change detection threshold across all biomes. A high chiSquareProbability of 0.99 was found to be essential for maintaining global stability; lower thresholds (e.g., 0.70-0.90) led to excessive over-segmentation by mistaking seasonal phenological fluctuations for true forest disturbances, resulting in a dramatic decrease in OA.

Finally, regarding spectral input selection (Fig. 8c), a comparative analysis of various band combinations reveals that the inclusion of the NBR consistently yields the highest OA across all biomes, with gains of 3.4%-7.8% over raw reflectance-

based models (Source). This demonstrates that NBR effectively enhances the signal-to-noise ratio in identifying stand-replacing disturbances by leveraging the sensitivity of shortwave infrared (SWIR) bands to canopy moisture and structural changes.

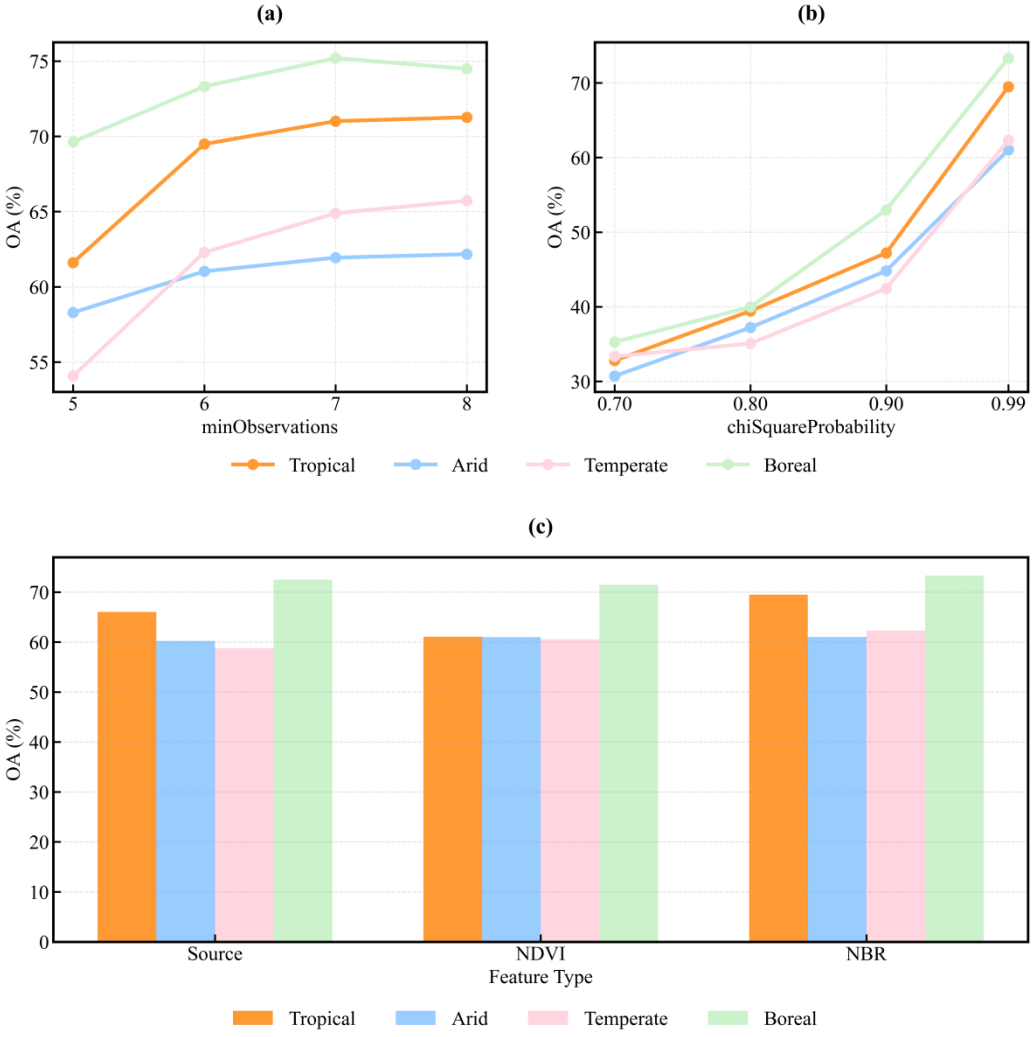

Figure 8: Sensitivity analysis of key temporal segmentation parameters and feature configurations across different climate zones. (a) OA sensitivity to minObservations; (b) OA sensitivity to chiSquareProbability under different climate zones; and (c) comparison of OA across feature configurations (Source, NDVI, and NBR) in different climate zones.

3.3 Global forest age spatial distribution characteristics

Globally, forest age exhibits distinct spatial patterns between NF and PF (Fig. 9). NF are broadly distributed across tropical, subtropical, and boreal regions, with older stands concentrated in the Amazon Basin, Central Africa, and northern Eurasia. These mature forests largely correspond to areas with minimal anthropogenic disturbance and long-term ecological stability.

In contrast, PF are predominantly distributed in the mid-latitudes, including East Asia, Europe, Australia, and southeastern South America, reflecting intensive forest management and large-scale reforestation efforts over recent decades (Bennett 2015). The global map reveals a clear latitudinal gradient: younger forests dominate economically developed and actively managed regions (e.g., East Asia, Europe, and parts of North America), while older stands prevail in equatorial and high-latitude zones. Compared with NF, PF exhibit a markedly younger age structure worldwide. Most PF areas fall within the 1-15-year range, particularly in China, Brazil, and the southeastern United States, where short-rotation plantation systems are common. In contrast, NF contain a substantially higher proportion of mature stands (>30 years), especially in remote tropical and Boreal climate zones dominated by natural succession. These spatial contrasts primarily stem from differences in forest management intensity, reforestation policies, and disturbance regimes. Younger PF ages in subtropical and temperate regions correspond to large-scale plantation rotations, whereas older NF ages in tropical and boreal areas reflect long-term ecological continuity. Compared with existing coarse-resolution products such as GAMI (100 m), the 30 m forest age map developed in this study provides a more detailed representation of spatial heterogeneity and better captures fine-scale age gradients across fragmented landscapes.

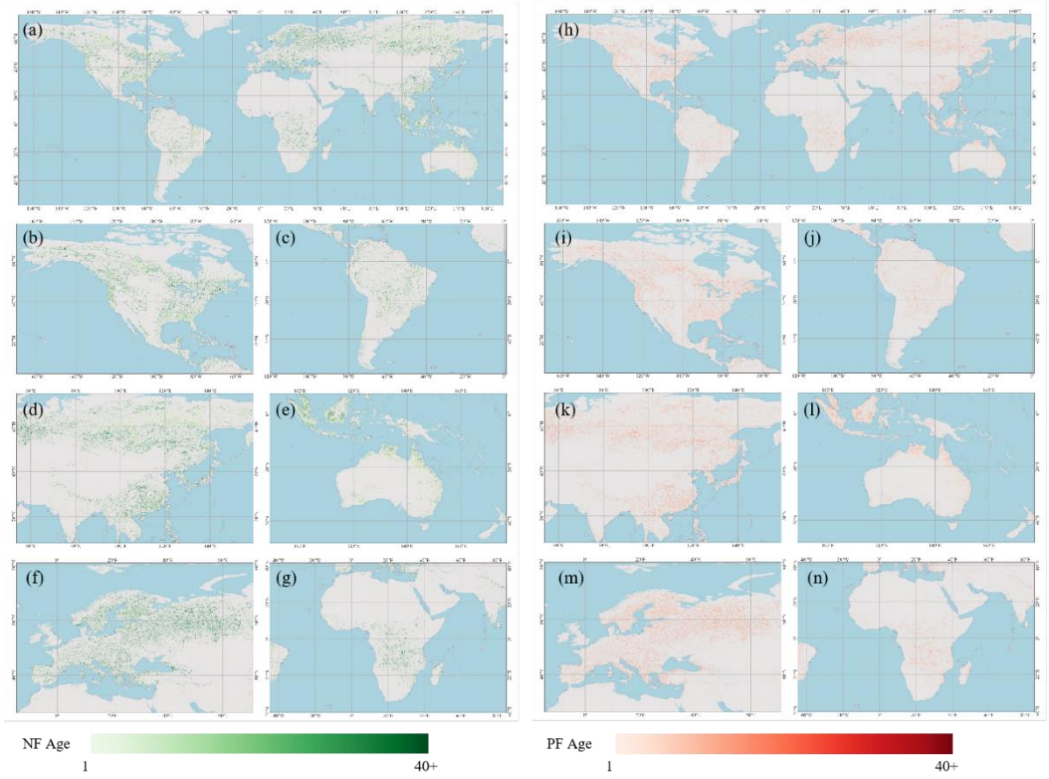

Figure 9: The distribution of global forest age. Natural forests (left) and planted forests (right). (a) presents the global spatial pattern of NF ages, with zoomed-in views of key regions including North America (b), South America (c), Asia (d), Australia (e), Europe (f), and Africa (g); (h) displays the global distribution of PF ages, complemented by zoomed-in views of North America (i), South America (j), Asia (k), Australia (l), Europe (m), and Africa (n).

3.4 Regional variations in age structure between planted and natural forests

Building upon the global spatial distribution patterns, we further quantified regional variations in the age structure of NF and PF across six continents—Africa, Asia, Australia, Europe, North America, and South America—to reveal their distinct developmental characteristics and management contexts.

The age structures of NF and PF exhibit pronounced regional contrasts (Fig. 10). For NF, Europe (84.38%), South America (82.61%), and North America (80.62%) show a predominance of the oldest age class (Age 36-40), each typically exceeding 80%. Africa (66.46%) and Asia (48.61%) follow this pattern, whereas Australia exhibits a notable bimodal pattern, with both young (Age 1-5: 31.36%) and old (Age 36-40: 35.64%) stands contributing substantially. Except for Australia, young NF (Age 1-10) occupy less than 8% across all other continents. Notably, Asia contains a relatively high proportion of middle-aged forests (Age 21-25: 21.95%), suggesting more active regeneration and a balanced age composition. PF, in contrast, are markedly younger across all continents. In Australia, PF are highly concentrated in the youngest class (Age 1-5: 65.77%), with only 8.12% in the oldest (Age 36-40). The young age structure is likely associated with the dominance of short-rotation species widely used in Australian plantations (Strandgard et al., 2021). Both Africa and South America exhibit a "young-and-old dual peak" structure—Africa (Age 1-5: 31.09%; Age 36-40: 36.60%) and South America (Age 1-5: 31.11%; Age 36-40: 32.59%). PF in North America (Age 1-5: 17.66%) and Asia (Age 1-5: 18.58%) are generally skewed toward younger stands, though older classes still represent 34.36% and 30.09%, respectively. Europe is the only region where old PF dominate (Age 36-40: 53.99%), while young PF remain below 20%. Regionally, PF in Australia, Asia, and North America are dominated by younger stands, Africa and South America exhibit mixed age compositions, and Europe is characterized by relatively mature plantation structures.

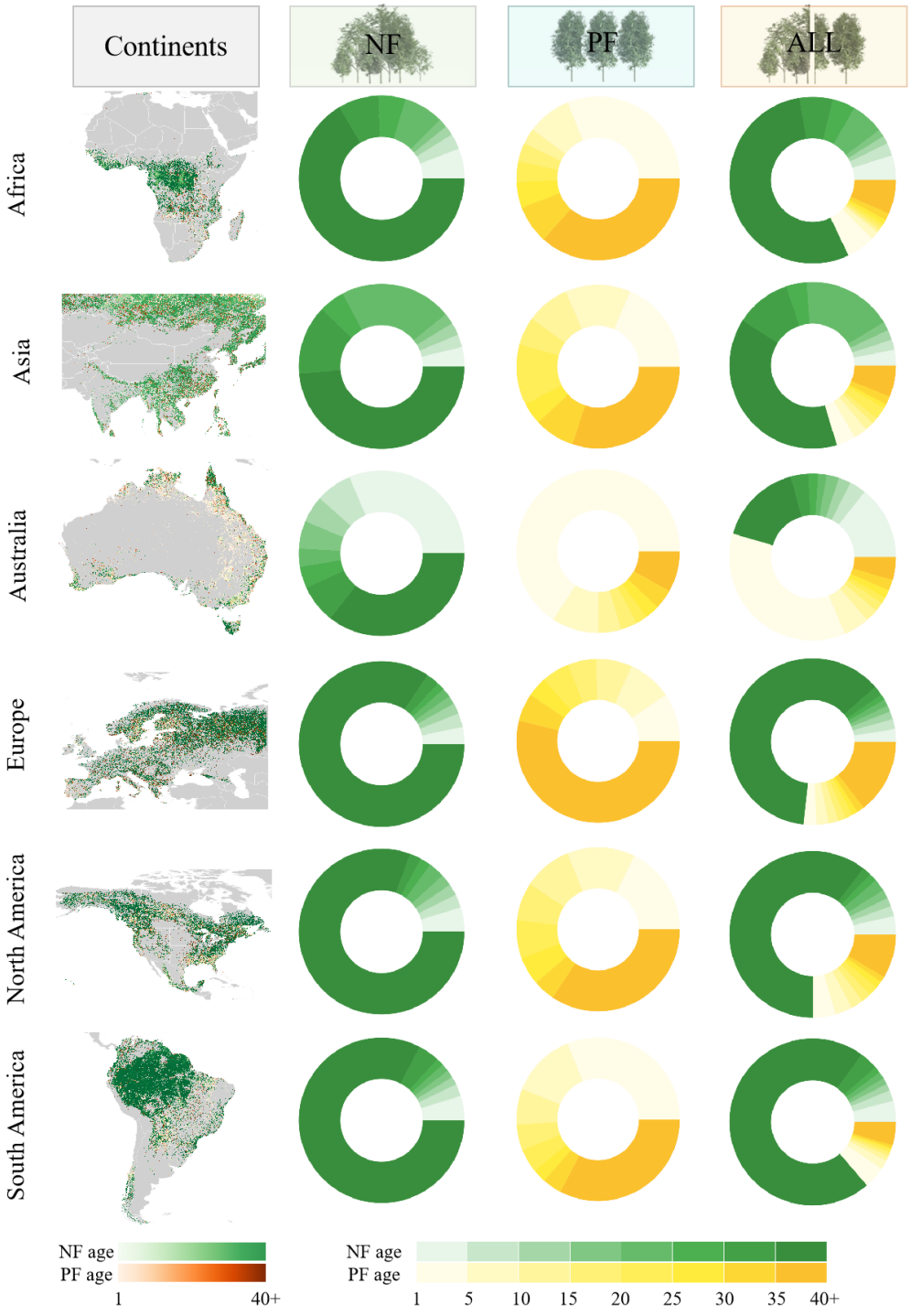

Figure 10: Regional age-class distributions of planted and natural forests across six continents. The first column shows the six global regions. The second and third columns depict the proportional distributions of NF and PF, respectively, across eight age classes (1-5 to 36-40 years, in 5-year intervals). The fourth column summarizes the total proportions of NF and PF within each region.

4 Discussion

4.1 Methodological standardization and parameter sensitivity

To evaluate the robustness of the CCDC-based forest age mapping framework, we conducted a systematic sensitivity analysis of two foundational hyperparameters—minObservations and chiSquareProbability—across four major ecological zones (Arid, Boreal, Temperate, and Tropical). The results indicate that classification accuracy generally improves with stricter statistical constraints, which enhance stability in breakpoint detection. Among the biomes, the Boreal region consistently yielded the highest overall accuracy, whereas the Arid region exhibited comparatively lower performance, primarily due to its inherently low vegetation cover and high background spectral variability (Almalki et al., 2022). In contrast, the Tropical and Boreal zones demonstrated the highest sensitivity to parameter tuning, implying that dense and structurally complex forest ecosystems are more responsive to breakpoint detection thresholds (DeVries et al., 2015).

The chiSquareProbability parameter reached optimal performance at 0.99 across all zones, indicating that a stringent statistical threshold is essential to suppress spurious breakpoints and minimize commission errors in disturbance detection (Fig. 8). Similarly, increasing minObservations improved model stability below a value of 6, beyond which the performance gains plateaued, identifying a distinct saturation threshold.

Beyond the global optimization of CCDC baseline hyperparameters, the implementation of the dual-threshold segment-fusion logic directly addresses a long-standing bottleneck in optical time-series forest age estimation: the systematic temporal lag between initial biophysical recovery and subsequent mathematical model convergence (Tian et al., 2023). Crucially, the tailored regrowth slope thresholds enforced in this study—>0.03 for NF and a more stringent >0.04 for PF—were not arbitrarily selected but were empirically derived as the statistical means computed directly from our extensive historical reference sample points. This data-driven differentiation aligns perfectly with the distinct eco-physiological characteristics and successional trajectories of the two forest origins. For NF, the statistically derived lower mean slope (>0.03) successfully accommodates the slow, stochastic nature of natural secondary succession, which is often heavily confounded by complex multi-layered canopy interactions and localized understory regeneration that blur the overstory spectral signals (Tian et al., 2015). Conversely, fast-growing plantation species exhibit highly synchronized and aggressive vegetative growth post-establishment. By enforcing the more stringent 0.04 threshold for PF, the framework effectively isolates the rapid biomass accumulation and intense canopy closure typical of intensive commercial species (e.g., *Eucalyptus* or *Pinus*) (Deng et al., 2020). This restriction is functionally vital to prevent the high model stability during early successional stages from prematurely triggering a breakpoint reset, thereby avoiding an artificial underestimation of the estimated stand age. Nevertheless, utilizing a single, globally uniform mean threshold for each forest origin introduces certain geographic limitations. By compressing multi-biome successional dynamics into global average constants, the framework inevitably overlooks intra-type variations driven by macroclimatic gradients. For instance, cold-constrained boreal NF or slow-growing arid plantations may display actual recovery slopes that fall slightly below these statistical means (0.03 or 0.04), potentially leading to localized omissions where successional segments fail to fuse (Han et al., 2021). Conversely, in hyper-productive wet tropical domains, natural regrowth

might be aggressive enough to surpass the 0.04 threshold, blurring the algorithmic distinction between NF and PF trajectories. While these generalized thresholds represent an objective trade-off to maintain global inter-comparability and suppress local noise, future iterations should explore climate-zonal adaptive thresholds to further capture the fine-grained geographical volatility of forest recovery rates.

Reconciling localized optimization with inter-regional comparability remains a primary challenge in global-scale mapping. Although our sensitivity analysis identified minor regional variations in optimal thresholds—such as the requirement for higher observation counts to mitigate cloud interference in tropical domains (Fig. 8a)—we intentionally maintained a uniform parameter framework (Table 2) to establish an objective global benchmark. Adopting regionally adaptive parameters frequently introduces artificial boundary discrepancies and spatial discontinuities, compromising the cross-regional baseline comparability. As emphasized in seminal large-scale mapping frameworks, employing an internally consistent approach with standardized operational configurations is imperative to filter out geographic definition variations and data input inconsistencies, ensuring that macro-scale characterizations remain robust and comparable across diverse biomes (Hansen et al., 2013). By employing a consistent configuration validated across four distinct biomes, we ensure that the global contrasts in forest age structure revealed in this study are empirical reflections of regional forest dynamics and management regimes.

4.2 Spatial uncertainty indexing and physical drivers

The spatial heterogeneity exhibited by the SUI (Fig. 6) is deeply coupled with the interactions between regional forest stand structures, environmental dynamics, and the time-series segment-fitting mechanism of the CCDC algorithm.

The exceptionally low uncertainty (SUI < 5) observed in regions like southeastern China can be attributed to the prominence of managed forests and plantation ecosystems. In these zones, uniform stand-replacing clear-cuts or large-scale planting events generate distinct, sharp spectral break-points, allowing the CCDC algorithm to fit subsequent regrowth trajectories with minimal residual noise. Meanwhile, the high-confidence cluster in the southwestern United States and subtropical southern Africa is primarily driven by atmospheric and climatic advantages. These arid and semi-arid regions feature persistently clear-sky conditions and sparse cloud cover, which guarantees a continuous and abundant volume of high-quality Landsat observations. The low seasonal complexity and minimal background noise in these dry ecosystems enable the CCDC time-series inversion to maintain exceptionally tight spectral trajectories, thereby minimizing fitting residuals.

Conversely, the moderate-to-high SUI values (8-13) captured across tropical rainforest domains (e.g., the Amazon Basin and Central Africa) and high-latitude zones (e.g., northern North America and northern Eurasia) are driven by contrasting environmental constraints. Persistent cloud cover in the tropics and high atmospheric moisture content often limit the acquisition frequency of noise-free optical data, inflating the fitting residuals. Furthermore, the multi-layered canopy structures and sub-pixel heterogeneity inherent to natural rainforests mean that partial disturbances often cause subtle spectral variations rather than clean resets, leading to elevated SUI values. Crucially, these localized compounding factors—where extreme data scarcity due to cloud contamination overlaps with intense sub-pixel canopy dynamics—further escalate the fitting error,

manifesting as the scattered pixel-level hot spots of maximum uncertainty (SUI > 12, appearing as yellow pixels) observed within the core tropical domains.

In higher latitudes, the maximum mapping uncertainty (SUI > 12) is driven by severe winter conditions. Prolonged snow cover, winter freezing, and intense seasonal phenological variations inject substantial baseline noise into the optical time-series data, inherently increasing the standard deviation of the spectral fitting residuals. This algorithmic behavior is firmly validated by our independent ground networks, where the Boreal climate zone exhibited the highest empirical error (MAE = 3.84 years), contrastingly mirroring the Tropical climate zone where the bounded baseline fitting noise successfully maintained a minimized actual mapping error (MAE = 1.15 years).

4.3 Systematic biases, conceptual lags, and dataset limitations

A rigorous evaluation of our validation results reveals a nuanced structure of estimation uncertainties across distinct forest developmental stages, as explicitly manifested in the joint plot of continuous estimations and probability densities across different observed age groups (Fig. 11). Contrasting with traditional empirical biomass-to-age models that typically suffer from progressive error expansion in mature cohorts, our CCDC-based framework exhibits highly constrained and narrowly binned probability distributions in the oldest cohort (30-40 years, Fig. 11). This exceptional convergence at the upper age limit directly mirrors the high UA (93.48%) reported in our cross-comparison matrix, demonstrating strong structural stability when delineating long-term undisturbed forest domains.

Nevertheless, a minor, vertically scattered trace of data points within this oldest green cohort extends downward toward the baseline (Fig. 11). This trailing underestimation represents a classic algorithmic artifact within long-term time-series segmentation, where anomalous, non-disturbance events—such as extreme localized drought, severe ephemeral frost, or residual cloud-shadow contamination—temporarily distort the spectral trajectory. Even under a stringent statistical constraint (chiSquareProbability = 0.99), these high-magnitude biophysical or radiometric anomalies can occasionally trigger spurious breakpoints, causing the CCDC model to misinterpret an undisturbed mature stand as a newly initiated segment and prematurely reset its estimated age.

Conversely, while the major responsive cohorts cluster acceptably within their corresponding reference boundaries, the intermediate successional stages—specifically the 10-20 and 20-30 year intervals—exhibit a relatively higher degree of structural volatility and a discernible downward tracking variance (Fig. 11). As illustrated by the noticeably widened interquartile ranges and the prolonged downward tails of the probability density clouds in these middle-aged binned groups, a non-negligible portion of samples are estimated below their true biological reference lines. The prominent downward dispersion in these 10-30 year stands reflects the complex spectral signatures of partial, low-intensity disturbances (e.g., selective logging, surface fires, or insect outbreaks). In these young-to-middle-aged NF, partial canopy removal often generates subtle spectral shifts rather than clean stand-replacing resets. The CCDC algorithm may occasionally misinterpret these subtle variations or subsequent rapid canopy closures as entirely new model initializations (t_{Start}), thereby artificially "resetting" the age of a mature stand to a few years and inflating the underestimation error. Acknowledging these segment-fitting sensitivities

within intermediate age intervals is crucial for downstream users applying this dataset to carbon sequestration modeling and forest structure dynamics.

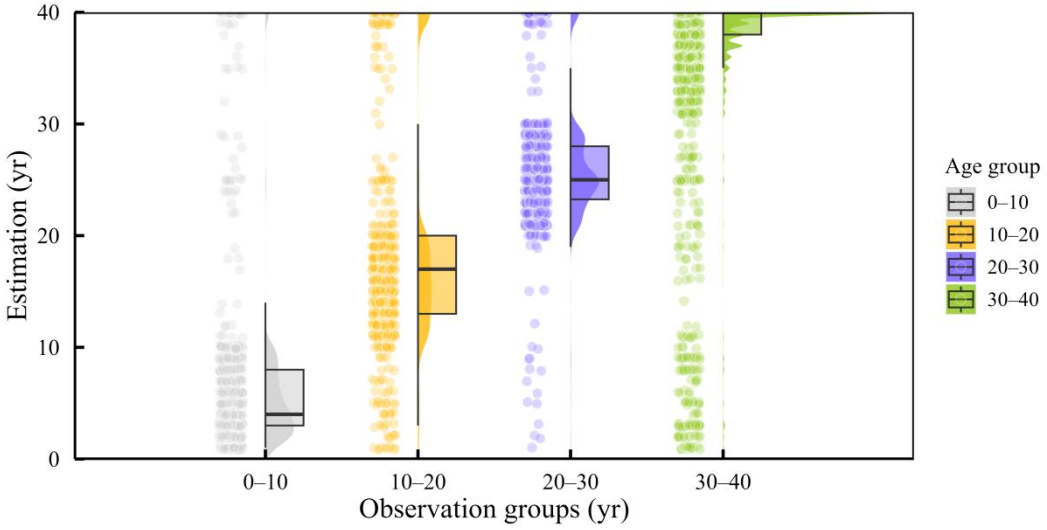

Figure 11: Distribution of estimated forest age for different observed age groups.

Beyond historical data depth and segment-fitting sensitivities, conceptual and algorithmic lags introduce minor systematic uncertainties. A technical nuance arises from the discrepancy between the algorithmic t_{Start} and the true biological onset of regrowth. Because the GEE implementation of CCDC requires a minimum number of valid observations to initialize a new stable model segment, the estimated t_{Start} inherently reflects the point of model convergence. This introduces a minor temporal lag—typically ranging from several months to a year depending on regional observation frequency. Beyond this algorithmic delay, an ecological lag phase exists between disturbance and tree establishment. In many ecosystems, the post-disturbance period is initially dominated by grasses and shrubs before tree cohorts become dominant. This implies that our estimated "stand age" (time since disturbance) may slightly exceed the actual "tree age." While this lag is relatively consistent within similar biomes and does not compromise the identified macro-spatial patterns, it carries significant implications for carbon cycle modeling, as carbon sequestration rates during early-successional shrub stages differ substantially from those in established young forest stands.

Additional localized uncertainties stem from phenological interference and sensor artifacts. In temperate and boreal biomes, the pronounced seasonality of deciduous species produces spectral signals (e.g., natural annual senescence and rapid spring green-up) that intrinsically overlap with the spectral signatures of disturbance and recovery. While the CCDC algorithm's harmonic regression model is designed to isolate these seasonal cycles, it may still struggle with atypical phenological shifts driven by extreme climatic events, leading to spurious breakpoint detections. Furthermore, in dense deciduous stands, rapid canopy closure during the first few growing seasons may saturate spectral indices like NBR before the stand reaches true structural stability. Finally, radiometric inconsistencies, particularly the scan line corrector (SLC)-off gaps in Landsat 7

imagery, locally distort spectral trajectories and introduce minor biases, notably manifested as image banding effects that disrupt time-series signal stability across certain African regions.

4.4 Advances over existing products and strategic management implications

Current global forest age products—such as GFAD, GAMI, and PYP—face inherent limitations in spatial resolution, regional adaptability, and the differentiation of natural and planted forests. Most existing datasets operate at coarse spatial resolutions (100 m) and typically do not distinguish forest origin, leading to mixed and often biased age estimates that obscure management-driven differences in forest dynamics. The 30 m GFAM-N/P developed in this study addresses these challenges by offering spatially explicit and origin-specific age estimates for NF and PF. This fine spatial detail enables the detection of subtle regional variations in age structure, particularly across heterogeneous landscapes where natural and planted forests are closely interwoven (Fig. 9). Comparative analyses highlight these improvements: our dataset captures fine-scale gradients absent from coarser products, while mitigating data gaps across regions like South America and Europe that are prevalent in biomass-driven or record-limited empirical models (e.g., GAMI and PYP, Fig. 12).

The pronounced spatial heterogeneity and structural contrasts between NF and PF revealed in this study underscore the necessity of shifting from generalized global forestry frameworks to region-specific, precision management strategies. In short-rotation plantation regions (e.g., Australia, parts of Africa, and Southeast Asia) dominated by young PF cohorts (1-15 years), extending rotation cycles and promoting mixed-species configurations could significantly enhance ecological resilience and long-term soil carbon stabilization. Conversely, in regions dominated by mature NF (e.g., Europe and North America) where stands frequently exceed 30 years, conservation frameworks should prioritize maintaining natural regeneration, structural diversity, and habitat continuity to sustain old-growth biodiversity and prevent massive carbon release from potential disturbances. Asia, characterized by a relatively balanced forest age composition, represents a critical transitional system where protection-oriented and productivity-driven strategies can harmoniously coexist. Ultimately, the high-resolution, origin-specific forest age data provided by GFAM-N/P offers a transparent, reproducible, and robust empirical foundation for optimizing global forest management, optimizing carbon budget accounting, and informing policy decisions that reconcile climate mitigation with sustainable socio-economic development.

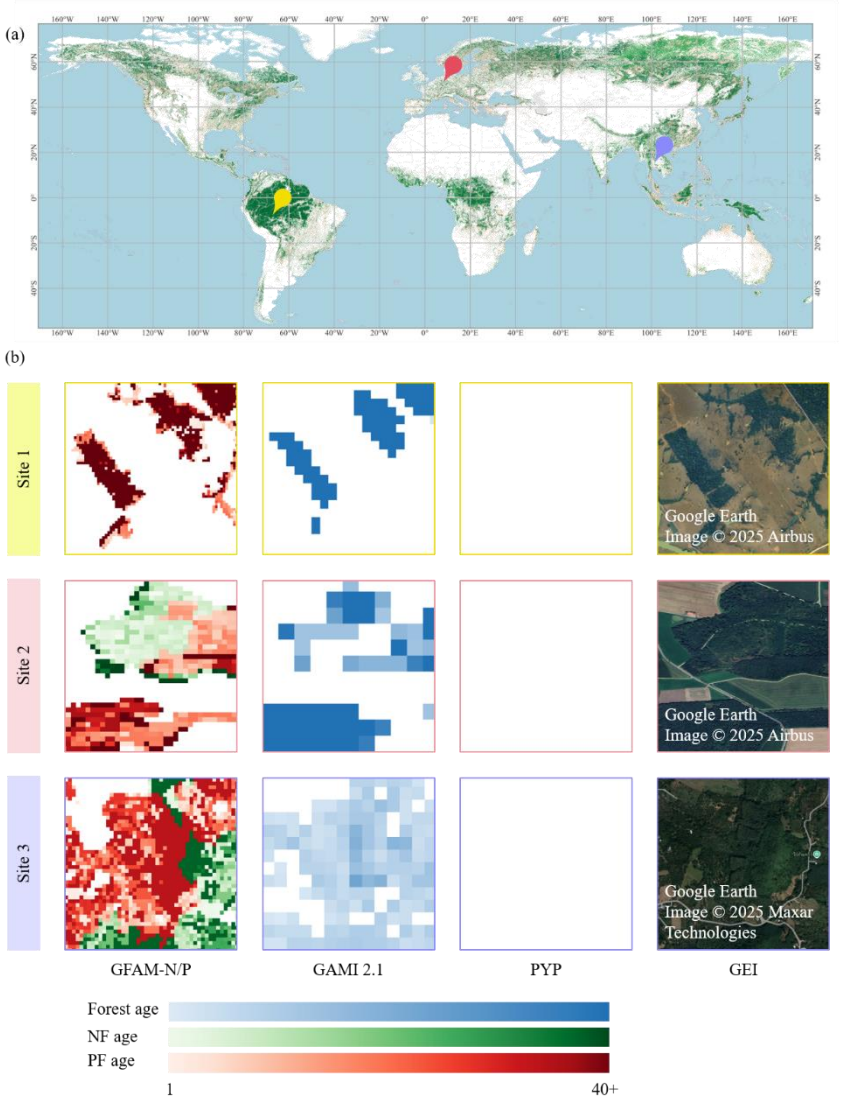

Figure 12: Comparison of global forest age products and demonstration of spatial improvements achieved in this study. (a) Global distribution of three representative validation sites used for product comparison. (b) Local comparisons among the GFAM-N/P, the GAMI 2.1 product, the planting year of plantations (PYP) dataset, and high-resolution Google Earth Imagery (GEI). The three sites represent heterogeneous forest landscapes across South America (Site 1), Europe (Site 2), and Southeast Asia (Site 3). Blank regions in the PYP column indicate areas with no available data. Note: High-resolution reference images in the GEI column are adapted from Google Earth with original attributions; underlying map material and imagery copyrights are provided and visible in the map (Imagery © 2025 Airbus and © 2025 Maxar Technologies).

5 Conclusion

Accurate mapping of forest ages is critical to advancing global carbon neutrality, as it underpins two core pillars of climate mitigation: carbon sink quantification and targeted forest management. Traditional approaches—reliant on labor-intensive

ground inventories—and existing coarse-resolution global forest age products fail to distinguish between PF and NF, severely limiting precise regional carbon accounting and evidence-based climate governance.

To address this critical gap, we developed a 30-m resolution global forest age dataset (GFAM-N/P) by integrating the CCDC model with multi-decadal Landsat time-series imagery on the GEE platform. Validated against an extensive network of multi-evidence interpretation samples and field survey plots, our framework demonstrated high predictive accuracy on a global scale, achieving an R^2 of 0.74 and an RMSE of 7.17 years. Furthermore, cross-comparison with independent datasets confirmed high spatial consistency, yielding an OA of 76.12% and a Kappa coefficient of 0.67.

By delivering high-resolution, forest-type-specific age estimates without relying on traditional static biomass inversions, this product fills a key niche in global ecosystem research, providing actionable data to advance ecosystem service assessment and process-based carbon cycle modeling. More importantly, it establishes a robust technical framework for regionally tailored forest management, enabling the refined implementation of global carbon neutrality commitments.

Author contributions

YW: Conceptualization, Methodology, Formal analysis, Investigation, Resources, Sampling, Data Curation, Writing, Visualization.

HW: Formal analysis, Investigation.

CL, XL: Resources, Sampling.

ZL, XZ, SL, JY: Supervision, Project administration.

YZ: Formal analysis, Investigation, Supervision, Project administration.

Competing interests

The authors declare that they have no conflict of interest.

Acknowledgements

We agree to include the standard disclaimer provided by Copernicus Publications. The manuscript does not involve any sensitive jurisdictional claims, and therefore no additional disclaimer text is required.

Financial support

Funding: This research was funded by the National Key Research and Development Program of China [grant number 2024YFD1500605.

Data availability

The primary dataset is hosted on Zenodo and can be accessed via https://doi.org/10.17632/yfm4sw8h25.1 (Wang et al., 2025).

References

[1] Almalki, R., Khaki, M., Saco, P.M., & Rodriguez, J.F. (2022). Monitoring and mapping vegetation cover changes in arid and semi-arid areas using remote sensing technology: A review. *Remote Sensing, 14*, 5143

[2] Aszalós, R., Thom, D., Aakala, T., Angelstam, P., Brūmelis, G., Gálhidy, L., Gratzer, G., Hlásny, T., Katzensteiner, K., Kovács, B., Knoke, T., Larrieu, L., Motta, R., Müller, J., Ódor, P., Roženbergar, D., Paillet, Y., Pitar, D., Standovár, T., Svoboda, M., Szwagrzyk, J., Toscani, P., & Keeton, W.S. (2022). Natural disturbance regimes as a guide for sustainable forest management in Europe. *Ecol Appl, 32*, e2596

[3] Bennett, B.M. (2015). *Plantations and protected areas: A global history of forest management*. MIT Press

[4] Besnard, S., Koirala, S., Santoro, M., Weber, U., Nelson, J., Gütter, J., Herault, B., Kassi, J., N'Guessan, A., & Neigh, C. (2021). Mapping global forest age from forest inventories, biomass and climate data. *Earth System Science Data Discussions, 2021*, 1-22

[5] Besnard, S., Santoro, M., Herold, M., Cartus, O., Gütter, J., Heinrich, V.H., Herault, B., Kassi, J., Koirala, S., N'Guessan, A., Neigh, C., Nelson, J.A., Poulter, B., Weber, U., Zhang, T., & Carvalhais, N. (2024). Global Age Mapping Integration (GAMI). In

[6] Bright, B.C., Hudak, A.T., Kennedy, R.E., Braaten, J.D., & Henareh Khalyani, A. (2019). Examining post-fire vegetation recovery with Landsat time series analysis in three western North American forest types. *Fire Ecology, 15*, 1-14

[7] Bunce, C. (2009). Correlation, agreement, and Bland–Altman analysis: statistical analysis of method comparison studies. *American journal of ophthalmology, 148*, 4-6

[8] Cao, Y., Zhong, D., Shang, R., Ke, Q., Zhang, M., Xie, D., Liu, S., Zhao, C., & Wei, R. (2025). Afforestation as a mitigation strategy: countering climate-induced risk of forest carbon sink in China. *Carbon Balance and Management, 20*, 18

[9] Champion, I., Germain, C., Da Costa, J.P., Alborini, A., & Dubois-Fernandez, P. (2013). Retrieval of forest stand age from SAR image texture for varying distance and orientation values of the gray level co-occurrence matrix. *IEEE Geoscience and Remote Sensing Letters, 11*, 5-9

[10] Chen, W., Chen, J., Liu, J., & Cihlar, J. (2000). Approaches for reducing uncertainties in regional forest carbon balance. *Global Biogeochemical Cycles, 14*, 827-838

[11] Cheng, K., Chen, Y., Xiang, T., Yang, H., Liu, W., Ren, Y., Guan, H., Hu, T., Ma, Q., & Guo, Q. (2024a). A 2020 forest age map for China with 30 m resolution. *Earth Syst. Sci. Data, 16*, 803-819

[12] Cheng, K., Yang, H., Tao, S., Su, Y., Guan, H., Ren, Y., Hu, T., Li, W., Xu, G., Chen, M., Lu, X., Yang, Z., Tang, Y., Ma, K., Fang, J., & Guo, Q. (2024b). Carbon storage through China's planted forest expansion. *Nat Commun, 15*, 4106

[13] Deng, X., Guo, S., Sun, L., & Chen, J. (2020). Identification of short-rotation eucalyptus plantation at large scale using multi-satellite imageries and cloud computing platform. *Remote Sensing, 12*, 2153

[14] DeVries, B., Decuyper, M., Verbesselt, J., Zeileis, A., Herold, M., & Joseph, S. (2015). Tracking disturbance-regrowth dynamics in tropical forests using structural change detection and Landsat time series. *Remote Sensing of Environment, 169*, 320-334

[15] Du, Z., Yu, L., Yang, J., Xu, Y., Chen, B., Peng, S., Zhang, T., Fu, H., Harris, N., & Gong, P. (2022). A global map of planting years of plantations. *Scientific data, 9*, 141

[16] Erdozain, M., Alberdi, I., Aszalós, R., Bollmann, K., Detsis, V., Diaci, J., Đodan, M., Efthimiou, G., Gálhidy, L., Haase, M., Hoffmann, J., Jaymond, D., Johann, E., Jørgensen, H., Krumm, F., Kuuluvainen, T., Lachat, T., Lapin, K., Lindner, M., Madsen, P., Nichiforel, L., Pach, M., Paillet, Y., Palaghianu, C., Palau, J., Pemán, J., Perić, S., Raum, S., Schueler, S., Skrzyszewski, J., Svensson, J., Teeuwen, S., Vacchiano, G., Vandekerkhove, K., Cañellas, I., Menéndez-Miguélez, M., Werden, L.L.K., Àvila, A., & de-Miguel, S. (2024). The Evolution of Forest Restoration in Europe: A Synthesis for a Step Forward Based on National Expert Knowledge. *Current Forestry Reports, 11*, 4

[17] Escuin, S., Navarro, R., & Fernández, P. (2008). Fire severity assessment by using NBR (Normalized Burn Ratio) and NDVI (Normalized Difference Vegetation Index) derived from LANDSAT TM/ETM images. *International Journal of Remote Sensing, 29*, 1053-1073
[18] FAO (2024). The State of the World's Forests. In
[19] Han, C., Liu, Y., Zhang, C., Li, Y., Zhou, T., Khan, S., Chen, N., & Zhao, C. (2021). Effects of three coniferous plantation species on plant-soil feedbacks and soil physical and chemical properties in semi-arid mountain ecosystems. *Forest Ecosystems, 8*, 3
[20] Hansen, M.C., Potapov, P.V., Moore, R., Hancher, M., Turubanova, S.A., Tyukavina, A., Thau, D., Stehman, S.V., Goetz, S.J., & Loveland, T.R. (2013). High-resolution global maps of 21st-century forest cover change. *science, 342*, 850-853
[21] He, G., Zhang, Z., Zhu, Q., Wang, W., Peng, W., & Cai, Y. (2022). Estimating Carbon Sequestration Potential of Forest and Its Influencing Factors at Fine Spatial-Scales: A Case Study of Lushan City in Southern China. *International Journal of Environmental Research and Public Health, 19*, 9184
[22] Huang, Z., Li, X., Du, H., Zou, W., Zhou, G., Mao, F., Fan, W., Xu, Y., Ni, C., & Zhang, B. (2023). An algorithm of forest age estimation based on the forest disturbance and recovery detection. *IEEE Transactions on Geoscience and Remote Sensing, 61*, 1-18
[23] Ju, J., Roy, D.P., Vermote, E., Masek, J., & Kovalskyy, V. (2012). Continental-scale validation of MODIS-based and LEDAPS Landsat ETM+ atmospheric correction methods. *Remote Sensing of Environment, 122*, 175-184
[24] Köhl, M., Neupane, P.R., & Lotfiomran, N. (2017). The impact of tree age on biomass growth and carbon accumulation capacity: A retrospective analysis using tree ring data of three tropical tree species grown in natural forests of Suriname. *PLoS One, 12*, e0181187
[25] Leng, Y., Li, W., Ciais, P., Sun, M., Zhu, L., Yue, C., Chang, J., Yao, Y., Zhang, Y., Zhou, J., Li, Z., Wang, X., Xi, Y., & Peng, S. (2024). Forest aging limits future carbon sink in China. *One Earth, 7*, 822-834
[26] Li, P., Li, H., Si, B., Zhou, T., Zhang, C., & Li, M. (2024). Mapping planted forest age using LandTrendr algorithm and Landsat 5–8 on the Loess Plateau, China. *Agricultural and Forest Meteorology, 344*, 109795
[27] Liang, B., Wang, J., Zhang, Z., Zhang, J., Zhang, J., Cressey, E.L., & Wang, Z. (2022). Planted forest is catching up with natural forest in China in terms of carbon density and carbon storage. *Fundamental Research, 2*, 688-696
[28] Liao, W., Ye, D., Yuan, R., Zhang, Y., & Deng, Q. (2023). Financial compensation for natural forest logging ban: Standard calculation based on willingness to accept. *Sci Prog, 106*, 368504221145563
[29] Lu, J., Huang, C., Schleeweis, K., Zou, Z., & Gong, W. (2025). Tree age estimation across the US using forest inventory and analysis database. *Forest Ecology and Management, 584*, 122603
[30] Maltman, J.C., Hermosilla, T., Wulder, M.A., Coops, N.C., & White, J.C. (2023). Estimating and mapping forest age across Canada's forested ecosystems. *Remote Sensing of Environment, 290*, 113529
[31] Maza, M., Lara, J.L., & Losada, I.J. (2021). Predicting the evolution of coastal protection service with mangrove forest age. *Coastal Engineering, 168*, 103922
[32] Mo, L., Crowther, T.W., Maynard, D.S., van den Hoogen, J., Ma, H., Bialic-Murphy, L., Liang, J., de-Miguel, S., Nabuurs, G.-J., Reich, P.B., Phillips, O.L., Abegg, M., Adou Yao, Y.C., Alberti, G., Almeyda Zambrano, A.M., Alvarado, B.V., Alvarez-Dávila, E., Alvarez-Loayza, P., Alves, L.F., Amaral, I., Ammer, C., Antón-Fernández, C., Araujo-Murakami, A., Arroyo, L., Avitabile, V., Aymard, G.A., Baker, T.R., Bałazy, R., Banki, O., Barroso, J.G., Bastian, M.L., Bastin, J.-F., Birigazzi, L., Birnbaum, P., Bitariho, R., Boeckx, P., Bongers, F., Boonman, C.C.F., Bouriaud, O., Brancalion, P.H.S., Brandl, S., Brearley, F.Q., Brienen, R., Broadbent, E.N., Bruelheide, H., Bussotti, F., Gatti, R.C., César, R.G., Cesljar, G., Chazdon, R., Chen, H.Y.H., Chisholm, C., Cho, H., Cienciala, E., Clark, C., Clark, D., Colletta, G.D., Coomes, D.A., Valverde, F.C., Corral-Rivas, J.J., Crim, P.M., Cumming, J.R., Dayanandan, S., de Gasper, A.L., Decuyper, M., Derroire, G., DeVries, B., Djordjevic, I., Dolezal, J., Dourdain, A., Engone Obiang, N.L., Enquist, B.J., Eyre, T.J., Fandohan, A.B., Fayle, T.M., Feldpausch, T.R., Ferreira, L.V., Finér, L., Fischer, M., Fletcher, C., Frizzera, L., Gamarra, J.G.P., Gianelle, D., Glick, H.B., Harris, D.J., Hector, A., Hemp, A., Hengeveld, G., Hérault, B., Herbohn, J.L., Herold, M., Hietz, P., Hillers, A., Honorio Coronado, E.N., Hui, C., Ibanez, T., Imai, N., Jagodziński, A.M., Jaroszewicz, B., Johannsen, V.K., Joly, C.A., Jucker, T., Jung, I., Karminov, V., Kartawinata, K., Kearsley, E., Kenfack, D., Kennard, D.K., Kepfer-Rojas, S., Keppel, G., Khan, M.L., Killeen, T.J., Kim, H.S., Kitayama, K., Köhl, M., Korjus, H., Kraxner, F., Kucher, D., Laarmann, D., Lang, M., Lewis, S.L., Li, Y., Lopez-Gonzalez, G., Lu, H., Lukina, N.V., Maitner, B.S., Malhi, Y., Marcon, E., Marimon, B.S., Marimon-Junior, B.H., Marshall, A.R., Martin, E.H., McCarthy, J.K., Meave, J.A., Melo-Cruz, O., Mendoza, C., Mendoza-Polo, I., Miscicki,

S., Merow, C., Mendoza, A.M., Moreno, V.S., Mukul, S.A., Mundhenk, P., Nava-Miranda, M.G., Neill, D., Neldner, V.J., Nevenic, R.V., Ngugi, M.R., Niklaus, P.A., Ontikov, P., Ortiz-Malavasi, E., Pan, Y., Paquette, A., Parada-Gutierrez, A., Parfenova, E.I., Park, M., Parren, M., Parthasarathy, N., Peri, P.L., Pfautsch, S., Picard, N., Piedade, M.T.F., Piotto, D., Pitman, N.C.A., Poorter, L., Poulsen, A.D., Poulsen, J.R., Pretzsch, H., Arevalo, F.R., Restrepo-Correa, Z., Richardson, S.J., Rodeghiero, M., Rolim, S.G., Roopsind, A., Rovero, F., Rutishauser, E., Saikia, P., Salas-Eljatib, C., Saner, P., Schall, P., Schelhaas, M.-J., Schepaschenko, D., Scherer-Lorenzen, M., Schmid, B., Schöngart, J., Searle, E.B., Seben, V., Serra-Diaz, J.M., Sheil, D., Shvidenko, A.Z., Da Silva, A.C., Silva-Espejo, J.E., Silveira, M., Singh, J., Sist, P., Slik, F., Sonké, B., Sosinski, E.E., Souza, A.F., Stereńczak, K.J., Svenning, J.-C., Svoboda, M., Swanepoel, B., Targhetta, N., Tchebakova, N., ter Steege, H., Thomas, R., Tikhonova, E., Umunay, P.M., Usoltsev, V.A., Valencia, R., Valladares, F., Van Bodegom, P.M., van der Plas, F., Van Do, T., van Nuland, M.E., Vasquez, R.M., Verbeeck, H., Viana, H., Vibrans, A.C., Vieira, S., von Gadow, K., Wang, H.-F., Watson, J.V., Werner, G.D.A., Wittmann, F., Woell, H., Wortel, V., Zagt, R., Zawiła-Niedźwiecki, T., Zhang, C., Zhao, X., Zhou, M., Zhu, Z.-X., Zo-Bi, I.C., & Zohner, C.M. (2024). The global distribution and drivers of wood density and their impact on forest carbon stocks. *Nature Ecology & Evolution, 8*, 2195-2212

[33] Murphy, B.A., Rollinson, C.R., Dietze, M.C., Staudhammer, C.L., VonHedemann, N.R., Schultz, C.A., Kleindl, W.J., & Desai, A.R. (2025). Insights into nature-based climate solutions: Managing forests for climate resilience and carbon stability. *Journal of Geophysical Research: Biogeosciences, 130*, e2024JG008391

[34] Noss, R.F. (1999). Assessing and monitoring forest biodiversity: a suggested framework and indicators. *Forest Ecology and Management, 115*, 135-146

[35] Oldekop, J.A., Rasmussen, L.V., Agrawal, A., Bebbington, A.J., Meyfroidt, P., Bengston, D.N., Blackman, A., Brooks, S., Davidson-Hunt, I., Davies, P., Dinsi, S.C., Fontana, L.B., Gumucio, T., Kumar, C., Kumar, K., Moran, D., Mwampamba, T.H., Nasi, R., Nilsson, M., Pinedo-Vasquez, M.A., Rhemtulla, J.M., Sutherland, W.J., Watkins, C., & Wilson, S.J. (2020). Forest-linked livelihoods in a globalized world. *Nature Plants, 6*, 1400-1407

[36] Pan, Y., Chen, J.M., Birdsey, R., McCullough, K., He, L., & Deng, F. (2011). Age structure and disturbance legacy of North American forests. *Biogeosciences, 8*, 715-732

[37] Poulter, B., Aragao, L., Adela, N., Bellassen, V., Ciais, P., Kato, T., Lin, X., Nachin, B., Luyssaert, S., Pederson, N., Peylin, P., Piao, S., Saatchi, S., Schepaschenko, D., Schelhaas, M., & Shivdenko, A. (2018). The global forest age dataset (GFADv1.0)

[38] Poulter, B., Aragão, L., Andela, N., Bellassen, V., Ciais, P., Kato, T., Lin, X., Nachin, B., Luyssaert, S., Pederson, N., Peylin, P., Piao, S., Pugh, T., Saatchi, S., Schepaschenko, D., Schelhaas, M., & Shivdenko, A. (2019). The global forest age dataset and its uncertainties (GFADv1.1). In: PANGAEA

[39] Racine, E.B., Coops, N.C., St-Onge, B., & Bégin, J. (2014). Estimating forest stand age from LiDAR-derived predictors and nearest neighbor imputation. *Forest Science, 60*, 128-136

[40] Reyes-Palomeque, G., Dupuy, J., Portillo-Quintero, C., Andrade, J., Tun-Dzul, F., & Hernández-Stefanoni, J. (2021). Mapping forest age and characterizing vegetation structure and species composition in tropical dry forests. *Ecological Indicators, 120*, 106955

[41] Ryu, J.-H., Han, K.-S., Hong, S., Park, N.-W., Lee, Y.-W., & Cho, J. (2018). Satellite-based evaluation of the post-fire recovery process from the worst forest fire case in South Korea. *Remote Sensing, 10*, 918

[42] Shang, R., Chen, J.M., Xu, M., Lin, X., Li, P., Yu, G., He, N., Xu, L., Gong, P., Liu, L., Liu, H., & Jiao, W. (2023). China's current forest age structure will lead to weakened carbon sinks in the near future. *The Innovation, 4*, 100515

[43] Shi, X., Wang, T., Lu, S., Chen, K., He, D., & Xu, Z. (2022). Evaluation of China's forest carbon sink service value. *Environmental Science and Pollution Research, 29*, 44668-44677

[44] Smolina, A., Illarionova, S., Shadrin, D., Kedrov, A., & Burnaev, E. (2023). Forest age estimation in northern Arkhangelsk region based on machine learning pipeline on Sentinel-2 and auxiliary data. *Scientific Reports, 13*, 22167

[45] Steel, E.A., Hinckley, T.M., Richards, W.H., & D'Amore, D.V. (2024). Chapter 3 - Forests then and now: managing for ecosystem benefits, services to humans, and healthy forests across scales. In S.G. McNulty (Ed.), *Future Forests* (pp. 49-64): Elsevier

[46] Strandgard, M., & Bland, M. (2021). Economics of forest biomass for bioenergy: Potential site preparation savings from coarse woody harvesting residue removal in a short-rotation Eucalyptus globulus (Labill.) plantation. *Silva Balcanica, 22*, 45-55

[47] Su, Y., Zhang, C., Ciais, P., Zeng, Z., Cescatti, A., Shang, J., Chen, J.M., Liu, J., Wang, Y.-P., & Yuan, W. (2023). Asymmetric influence of forest cover gain and loss on land surface temperature. *Nature Climate Change, 13*, 823-831
[48] Systems, U.S.D.o.S.s.O.o.t.G.a.G.P. (2017). LSIB 2017: Large Scale International Boundary Polygons, Simplified. In
[49] Tang, S., Tian, Q., Xu, K., Xu, N., & Yue, J. (2020). Age information retrieval of Larix gmelinii forest using Sentinel-2 data. *Natl. Remote Sens. Bull, 24*, 1511-1524
[50] Terrell, G.R., & Scott, D.W. (1992). Variable kernel density estimation. *The Annals of Statistics*, 1236-1265
[51] Thompson, I., Mackey, B., McNulty, S., & Mosseler, A. (2009). Forest resilience, biodiversity, and climate change. In, *Secretariat of the Convention on Biological Diversity, Montreal. Technical Series no. 43. 1-67.* (pp. 1-67)
[52] Tian, H., Zhu, J., Lei, X., Jian, Z., Chen, X., Zeng, L., Huang, G., Liu, C., & Xiao, W. (2024). Models considering the theoretical stand age will underestimate the future forest carbon sequestration potential. *Forest Ecology and Management, 562*, 121982
[53] Tian, L., Liao, L., Tao, Y., Wu, X., & Li, M. (2023). Forest age mapping using landsat time-series stacks data based on forest disturbance and empirical relationships between age and height. *Remote Sensing, 15*, 2862
[54] Tian, X., Van der Tol, C., Su, Z., Li, Z., Chen, E., Li, X., Yan, M., Chen, X., Wang, X., & Pan, X. (2015). Simulation of forest evapotranspiration using time-series parameterization of the Surface Energy Balance System (SEBS) over the Qilian Mountains. *Remote Sensing, 7*, 15822-15843
[55] Trisasongko, B., Panuju, D., & Iman, L. (2020). Estimating tree age of rubber stands using spaceborne L-band synthetic aperture radar. In, *IOP Conference Series: Earth and Environmental Science* (p. 012079): IOP Publishing
[56] USDA Forest Service (2024). Forest Inventory and Analysis Database: FIA DataMart. In
[57] Vermote, E., Roger, J.-C., Franch, B., & Skakun, S. (2018). LaSRC (Land Surface Reflectance Code): Overview, application and validation using MODIS, VIIRS, LANDSAT and Sentinel 2 data's. In, *IGARSS 2018-2018 IEEE International Geoscience and Remote Sensing Symposium* (pp. 8173-8176): IEEE
[58] Vilén, T., Gunia, K., Verkerk, P., Seidl, R., Schelhaas, M.-J., Lindner, M., & Bellassen, V. (2012). Reconstructed forest age structure in Europe 1950–2010. *Forest Ecology and Management, 286*, 203-218
[59] Wang, Y., Wang, H., Liang, C., Li, X., Liu, Z., Zhang, X., Li, S., Yang, J., & Zhao, Y. (2025). The Global 30 m Forest Age Map (Natural vs. Planted Forest). In
[60] Xiao, Y., Wang, Q., Tong, X., & Atkinson, P.M. (2023). Thirty-meter map of young forest age in China. *Earth Syst. Sci. Data, 15*, 3365-3386
[61] Xiao, Y., Wang, Q., & Zhang, H.K. (2024). Global Natural and Planted Forests Mapping at Fine Spatial Resolution of 30 m. *Journal of Remote Sensing, 4*, 0204
[62] Yu, Z., Liu, S., Li, H., Liang, J., Liu, W., Piao, S., Tian, H., Zhou, G., Lu, C., & You, W. (2024). Maximizing carbon sequestration potential in Chinese forests through optimal management. *Nature communications, 15*, 3154
[63] Zhang, J., Zhang, P., Wang, R., Liu, Y., & Lu, S. (2023). Identifying the coupling coordination relationship between urbanization and forest ecological security and its impact mechanism: Case study of the Yangtze River Economic Belt, China. *Journal of Environmental Management, 342*, 118327
[64] Zhang, Y., Yao, Y., Wang, X., Liu, Y., & Piao, S. (2017). Mapping spatial distribution of forest age in China. *Earth and Space Science, 4*, 108-116
[65] Zou, H., & Song, Y. (2023). Influence of forest vegetation restoration on carbon increment after mining. *Scientific Reports, 13*, 19565